2013-02-05

Directional Electric Field Sensing Using Slab Coupled Optical Fiber Sensors

Daniel Theodore Perry
Brigham Young University - Provo

Directional Electric Field Sensing Using Slab Coupled Optical Fiber Sensors

Daniel Theodore Perry

A thesis submitted to the faculty of
Brigham Young University
in partial fulfillment of the requirements for the degree of

Master of Science

Stephen M. Schultz, Chair
Richard H. Selfridge
Aaron R. Hawkins

Department of Electrical and Computer Engineering

Brigham Young University

December 2012

ABSTRACT

Directional Electric Field Sensing Using Slab Coupled Optical Fiber Sensors

Daniel Theodore Perry
Department of Electrical and Computer Engineering, BYU
Master of Science

This thesis provides the details of a multi-axis electric field sensor. The sensing element consists of three slab coupled optical fiber sensors that are combined to allow directional electric field sensing. The packaged three-axis sensor has a small cross-sectional area of 0.5 cm x 0.5 cm achieved by using an x-cut crystal. The method is described that uses a sensitivity-matrix approach to map the measurements to field components. The calibration and testing are described resulting in an average error of 1.5º.

This work also includes a description of the packaging method used as well as a thorough analysis of the directional sensitivity of potassium titanyl phosphate (KTP) and electro-optic polymer: the two materials used as sensing elements. Each of the two materials is highly direction sensitive creating minimal crosstalk between the sensors.

Keywords: optics, fiber optics, D-fiber, electric field sensors

ACKNOWLEDGEMENTS

I would like to thank my wife for all of the support she has given me over the course of my research. Without her support completing my thesis would have been much more difficult. Her example of dedication and hard work has been an inspiration to me.

I also would like to thank my advisors, Dr. Schultz and Dr. Selfridge, for all of the time and effort they have spent helping guide my research. They have spent countless hours debugging problems, reading drafts, and teaching me which has allowed me to become a better student and researcher. Their support has been invaluable.

In the optics lab I have also had the opportunity to work with many other students who have significantly helped me in my research. They have provided great feedback and motivation along with significant contributions in testing and fabrication.

Finally I would like to thank Brigham Young University for giving me the opportunity to study and learn at their great institution. The lessons I learned from my professors and friends while attending BYU have helped shaped me into a better more developed person.

TABLE OF CONTENTS

LIST OF FIGURES

1 INTRODUCTION

1.1 Electric Field Sensing

An important application of electric field sensing is the safeguarding of sensitive electronics from a high powered microwave (HPM) and electromagnetic pulse (EMP) attacks. These weapons emit short, high-powered, high-frequency pulses that couple with conductive lines in electronics and inducing large currents that destroy the electronics [1-4]. The weapons have the ability to quickly disable all electronics in an area removing an area of all modern machinery and electronics.

To protect electronics from HPM and EMP attacks different forms of shielding have been developed. Shielding often involves encasing the electronics in metal casing or mesh to impede an applied electric field [5]. The efficacy of the shielding is determined by placing an electric field sensor inside of the shielding. To detect the electric field inside of the shielding the sensor must be non-perturbing, small, and direction sensitive.

Traditional electric field sensors, such as the D-dot sensor pictured in Figure 1-1, are large and metallic preventing their use in HPM and EMP testing [6]. When placed inside of metallic shielding, the metal power feed creates an electrical path through the shielding reducing the ability of the shielding to stop the electric field. The metal sensing element also changes how the electric field acts inside of the shielded cavity leading to an inaccurate measurement.

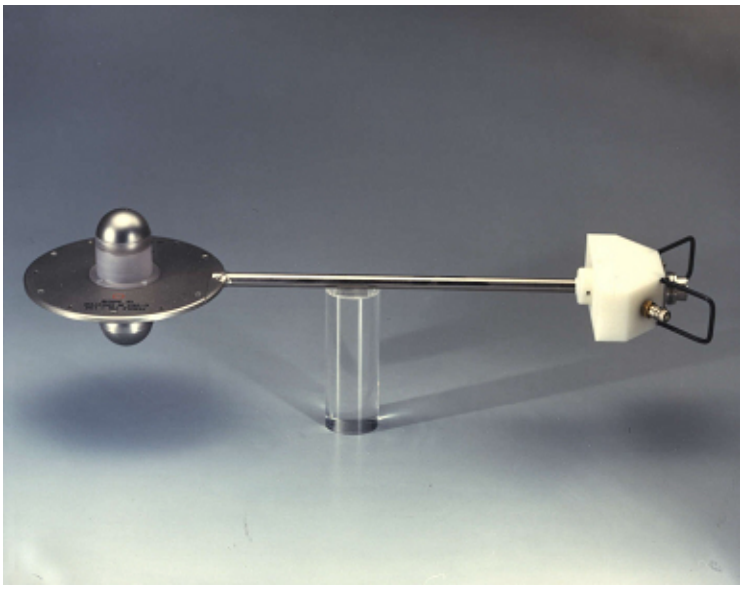

Figure 1-1: A photograph of a D-dot sensor [7].

In order for a sensor to be effective inside of the shielding it must be (1) non-metallic to avoid disrupting any electric field that penetrates the shielding, (2) small in sensing size to allow for high spatial resolution, and (3) directional to measure the full three-axis field direction and amplitude. Electric field sensors that can be used inside a shielded cavity include Mach-Zehnder, polarametric, and slab coupled optical fiber sensors.

1.1.1 Sensor Selection

Mach-Zehnder interferometers can be used to detect the strength of an electric field by splitting the light path into two paths and running each path through an electro-optic material such as lithium niobate before recombining the signal [8]. Applying an electric field causes a phase change between the paths resulting in destructive interference and power loss when the beams are recombined. The change in output power is dependent upon the strength of the electric field causing the phase change.

Polarimetric sensors work by injecting a 45° linearly polarizer light source into a birefringent fiber. The output of the fiber is passed through an analyzer and the relative power output is detected. These sensors have been adapted to electric field sensing [9] by using a medium in the fiber that is sensitive to electric fields. The power change at the end of the fiber will be different based on the extra rotation caused be the electric field.

Slab coupled optical fiber sensors (SCOS) [10] consist of an electro-optic slab waveguide placed in close proximity to the optical fiber core. The coupling of light between the core of the optical fiber and the electro-optic slab waveguide depends on the applied electric field. The resulting sensor is a relatively small dielectric sensor that provides low perturbation [10-13] and high bandwidth [13-15].

All three sensor types are dielectric so they do not provide a metallic path through shielding and also do not significantly disrupt any electric field that passes through the shielding. Mach-Zehnder and polarimetric sensors have large sensing elements because they need to allow distance for noticeable phase shift to occur. SCOS sensors can have sensing elements that are around 1mm long giving much better spatial resolution. None of the three sensor types are directional and alone are not capable of detecting the direction of the electric field.

1.2 **Contributions**

SCOS devices fulfill two of the requirements for sensing inside of shielded cavities in that they are dielectric and have high spatial resolution. A single SCOS sensor cannot measure the full three-axis direction. An individual SCOS device is direction sensitive causing the reported electric field to lessen when the sensing element is not parallel to the electric field. In an unknown environment this creates ambiguity in the measurement [16] because the direction

of the electric field is not known. When using three SCOS sensors together, however, the directional sensitivity of each SCOS device becomes advantageous. Mounting the sensing elements of three SCOS devices orthogonally to each other allows each sensor to detect only a portion of the entire electric field. The detected components are then used to determine the overall direction of the electric field. For this to work effectively the each sensor needs to be small so that the three sensing elements can be close together and the sensors need to be non-perturbing so that one sensor do not block the electric field from reaching the other two sensors.

I fabricated a three axis SCOS sensor and determined how to extract the electric field from the detected components output by each sensor. The absolute average error of the sensor is 1.26° with a cross sectional area of 0.5 cm x 0.5 allowing it to be placed in small areas and is non-perturbing allowing it to be used in shielded environments.

Knowing the theory and background behind SCOS is helpful when working with them. I will provide background on the SCOS devices including the fabrication process and theory about the operating principles for SCOS devices. Then the sensor I created is presented along with the experimental results.

2 SCOS BACKGROUND

SCOS devices take advantage of the linear optic effect (Pockel's effect) to detect electric fields. This effect is manifest in materials by a change of refractive index when an electric field is applied. Using a SCOS device, the magnitude of the change is determined and used to compute the strength of the electric field penetrating the material.

2.1 SCOS Operation

Figure 2-1 shows that SCOS consist of a D-fiber (KVH Industries) platform and a dielectric slab glued to the flat surface of the D-fiber. Light traveling through the fiber couples into the dielectric waveguide.

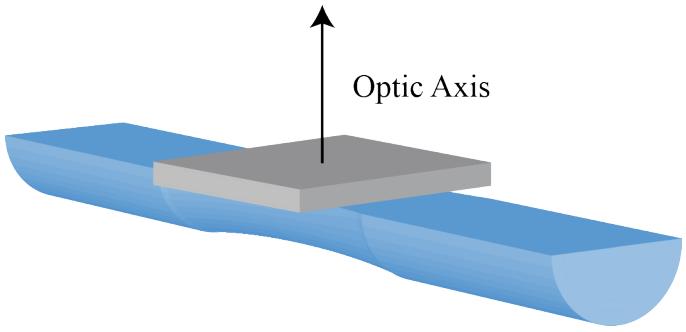

Figure 2-1: A linear optic waveguide attached to an etched D-fiber forming the basis for a SCOS device

In order for coupling between the waveguides to occur, two requirements need to be met. First, the waveguides need to be close enough so that the evanescent fields overlap. This occurs by placing the dielectric waveguide close to the core of the fiber. Second, constructive interference between the fiber mode and a waveguide mode needs to occur. Constructive interference between the two modes will only occur when the effective indices of the two modes are matched.

The core in the D-fiber is located approximately 13 μm from the flat side of the fiber. This distance needs to be about 1.5 μm for evanescent fields to overlap meaning cladding must be removed from the flat side of the fiber. This is accomplished using a hydrofluoric acid etch [17]. The etch removes enough of the cladding to expose the evanescent field and due to the D shape of the fiber leaves the fiber structurally intact.

The dielectric slab waveguide has many modes that dramatically change in effective index as the wavelength of the propagating light changes. The single mode optical fiber contains only a single mode that has only minimal change with wavelength. Coupling occurs when the effective indices are equal and occurs at wavelengths given by [18]

$$\lambda_m = \frac{2t}{m}\sqrt{{n_0}^2 - {N_f}^2}, \tag{2-1}$$

where n_0 is the index of refraction of the slab waveguide, N_f is the effective index of the fiber (1.451 for D-fiber at 1550nm), t is the thickness of the waveguide, and m is the mode number. As the equation implies, the wavelengths at which resonance dips occur are based on the refractive index of the slab waveguide. The strength of the coupling is dependent upon the distance between the waveguides and the length of the interaction region [19] and is quantified with the coupling coefficient, κ.

Figure 2-2a shows light coupling out of the optical fiber and into the slab [10] and Figure 2-2b shows the transmission spectrum. The transmission spectrum has resonant dips at the wavelengths where coupling occurred. Light that couples into the slab waveguide is not present in the transmission spectrum of the SCOS.

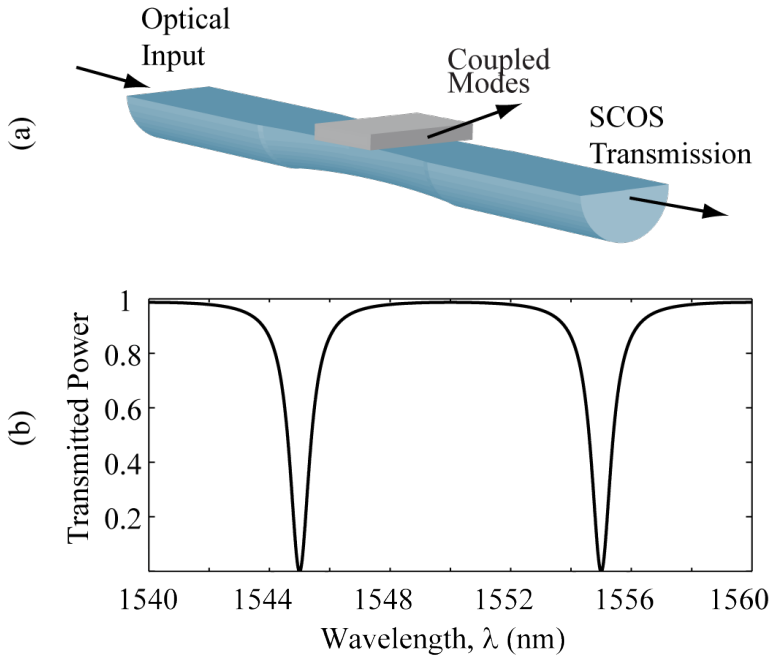

Figure 2-2: (a) SCOS showing optical input into D-fiber. (b) SCOS transmission spectrum showing resonant modes.

The slab waveguide is composed of a linear electro-optic material. Materials that lack a center of charge symmetry flex slightly when placed in an electric field. Changing the crystal structure of the material causes a change in refractive index. Changing the refractive index of the dielectric waveguide changes which wavelengths couple out of the fiber and consequently, the wavelength of the resonant dips. The strength of the electric field is determined by tracking the intensity at a particular wavelength as the index changes. Then the intensity change is mapped to field strength.

The magnitude of the index change is based on three different factors: the electro-optic coefficient of the waveguide, the index of refraction of the waveguide, and the strength of the electric field in which the waveguide is placed. The change is expressed as

$$\Delta n_0 = \frac{1}{2} {n_0}^3 r_{eff} E_{slab}, \tag{2-2}$$

where Δn_0 is the change is refractive index of the waveguide, n_0 is the index of the waveguide, r_{eff} is the combined electro-optic coefficient of the waveguide, and E_{slab} is the electric field in the waveguide.

The n_0 and r_{eff} terms are dependent upon the material properties of the slab. SCOS devices use anisotropic materials as the slab waveguide. Anisotropic materials have a different index of refraction in one of the three axial directions called the optic axis. The n_0 and r_{eff} terms are dependent on the direction of the applied field electric field, the direction of propagation of the wave, and the polarization of the propagating wave in anisotropic materials.

Light coupling into the dielectric slab waveguide does so at an angle determined by

$$\alpha = sin^{-1}\left(\frac{N_f}{n_0}\right). \tag{2-3}$$

Figure 2-3 shows light from the optical fiber coupling into the slab waveguide at an angle α relative to the principle axis. From a ray optics point of view, light traversing the slab at an angle to the principle axis is exposed to a component of the optic axis and normal axis causing the index of refraction to be given by

$$n_0 = \frac{n_x n_z}{\sqrt{n_x^2 sin^2(\alpha) + n_z^2 cos^2(\alpha)}} = \frac{n_{z'} n_{y'}}{\sqrt{n_{z'}^2 sin^2(\alpha) + n_{y'}^2 cos^2(\alpha)}}, \tag{2-4}$$

where n_x is the refractive index of waveguide in the x direction, n_y is the refractive index of the waveguide in the y direction, and n_z is the refractive index of the waveguide in the z direction.

The n_x and n_z terms are dependent upon the orientation of the slab waveguide relative to the D-fiber. When the geometry is the same as is pictured in Figure 2-3 with the x' axis of the crystal parallel to the global x axis and the y' axis of the crystal parallel to the global z axis, the equation takes the form on the right side of Equation (2-4). To determine n_0 and α of the slab waveguide, Equations (2-3) and (2-4) are solved simultaneously [20].

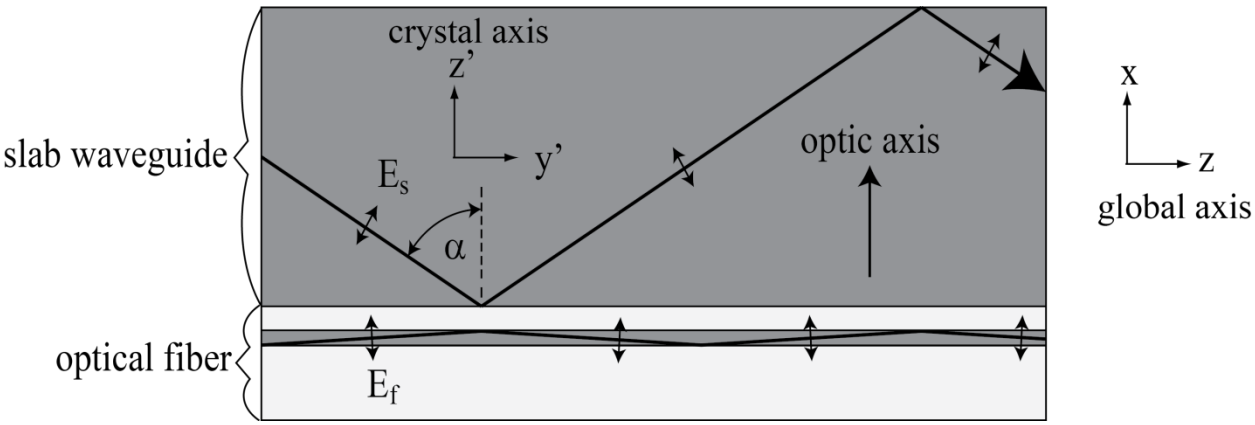

Figure 2-3: Angle that light couples into the electro-optic waveguide

The r_{eff} that the light "sees" is a combination of the r_x and the r_z terms of the linear optic tensor for the waveguide and is given by

$$r_{eff} = \frac{r_x r_z}{\sqrt{r_x^2 sin^2(\alpha) + r_z^2 cos^2(\alpha)}} = \frac{r_{23} r_{33}}{\sqrt{r_{23}^2 sin^2(\alpha) + r_{33}^2 cos^2(\alpha)}}. \quad (2\text{-}5)$$

r_{eff} is also dependent upon the orientation of the slab waveguide to the fiber. Again using the geometry pictured in Figure 2-3 the equation becomes what is shown on the right side of Equation (2-5).

The electric field changes while dropping over a dielectric slab based on electric field boundary conditions. For tangential electric fields the electric field is continuous on both sides of the boundary and for normal electric fields flux is continuous. The combination of these

conditions causes the electric field to be scaled inside of the dielectric slab. The electric field present in the slab is dependent upon the relative permittivity of the slab and the strength of the external electric field. It is determined for one orientation using [21]

$$E_{slab} = \frac{3}{\varepsilon_{slab} + 2} E, \tag{2-6}$$

where ε_{slab} is the relative permittivity of the slab and E is the electric field surrounding the slab.

Since n_0 and r_{eff} are constants for each SCOS device, the only variable in Equation (2-2) is the strength of the electric field showing that the magnitude of the index change is directly proportional to the strength of the electric field surrounding the waveguide.

2.2 SCOS Interrogation

To determine the magnitude of the index change in the slab waveguide, the SCOS device is interrogated using a tunable laser, optical detector, and an oscilloscope. The configuration is shown in Figure 2-4. The tunable laser provides a light source for the SCOS and is tuned to the "steep" section of the one the resonance dips in the transmission spectrum. The optical detector detects the transmitted light signal and changes it into a current which is amplified and displayed on the oscilloscope.

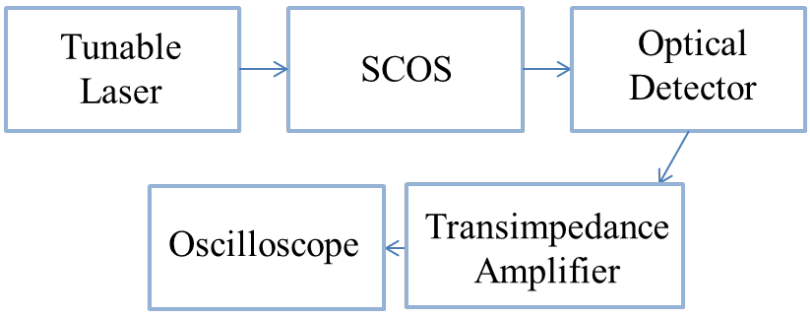

Figure 2-4: A block diagram of the setup to interrogate a SCOS device

A change in the refractive index of the slab waveguide causes a shift in the transmission spectrum of the SCOS. In Figure 2-5 a single resonance dip is picture along with the shift that results from an applied electric field. With the laser tuned to the edge of the resonance the amount of transmitted power changes when the spectrum shifts, which is shown by ΔT in Figure 2-5. Since the wavelength shift of the resonance is proportional to the applied field, the change in the power can be used to determine the amplitude of the electric field.

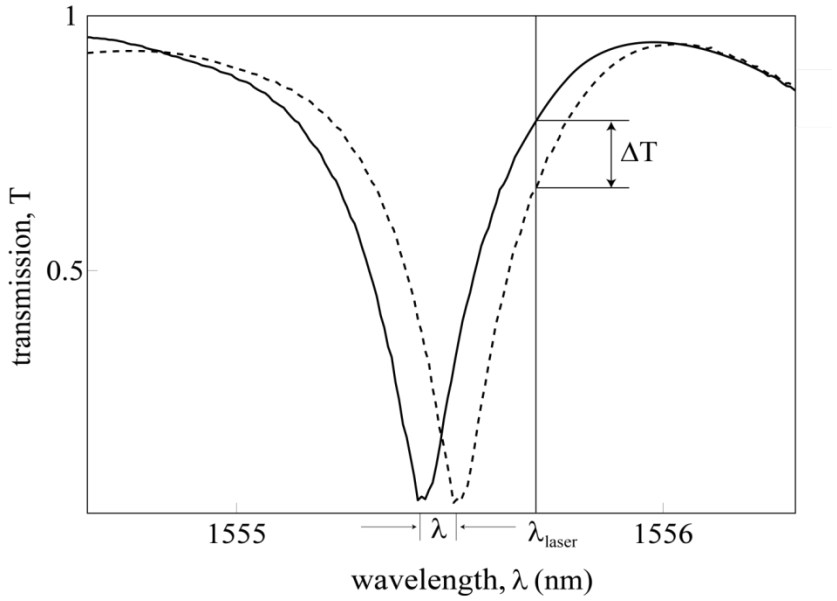

Figure 2-5: The transmission spectrum of a SCOS showing power shift due to an electric field

The power at the output of the SCOS changes corresponding to the shift in the transmission. An optical detector at the output of the SCOS device detects this power change and is given by

$$P_{rec} = P_t\left(T_0 + \frac{\Delta T}{E}E\right), \tag{2-7}$$

where P_{rec} is the power received by the detector, P_t is the optical signal strength, T_0 is the transmission coefficient without an applied electric field, ΔT is the change in transmission coefficient with an applied electrid field, and E is the strength of the electric field.

The optical detector converts the received power into a voltage which is then amplified and read on an oscilloscope. Measured voltage becomes a function of the strength of the electric field and is given by

$$V_{rec} = \left(\frac{\Delta P}{E}\right) RGE = CE, \tag{2-8}$$

where R is the responsitivity of the photo detector, G is the gain of the amplifier, and $\Delta P = P_t \Delta T$ is the change in power, and C is the calibration factor that relates the measured voltage to the applied electric field. The recieved power is directly proportional to the strength of the electric field enabling the strength of the electric field to be determined.

2.3 **SCOS Sensitivity**

The sensitivity of the SCOS is based on the resonance shift of the waveguide when it is placed inside of an electric field (the ΔT and E terms in (2-7)). The two primary components that contribute to the change in the transmission coefficient for a given applied electric field are the slope of the resonance ($\Delta T / \Delta \lambda$), and the shift in the resonant wavelength with applied electric field ($\Delta \lambda / E$).

For parallel waveguide directional couplers the transmission coefficient is given by [22]

$$T = 1 - \frac{\kappa^2}{\left(\kappa^2 + \left(\frac{\pi}{\lambda}\right)^2 \left(N - N_f\right)^2\right)^2}, \tag{2-9}$$

where the coupling coefficient, κ, is assumed to be identical between both waveguides and N and N_f are respectively the mode indices of the EO slab waveguide and the D-fiber. The slope of the transmission coefficent is found by taking the derivative of (2-9) with respect to N, resulting in

$$\frac{\Delta T}{\Delta N} = \frac{2\left(\kappa\frac{\pi}{\lambda}\right)^2 (N - N_f)}{\left(\kappa^2 + \left(\frac{\pi}{\lambda}\right)^2 (N - N_f)^2\right)^2}. \tag{2-10}$$

The slope can be increased by reducing the coupling coefficient (increasing the separation between the D-fiber core and the slab waveguide); however, weaker coupling requires a longer interaction length and is more sensitive to loss and EO slab uniformity. Therefore, there is a limit to the effectiveness of decreasing the coupling coefficient κ.

Since the mode indices of the waveguides need to be matched for resonant coupling, the mismatch in waveguide dispersion causes the resonance to be wavelength sensitive. A larger difference in the dispersion between the two waveguides causes the resonance to be steeper and thus the SCOS to be more sensitive.

2.4 **SCOS Fabrication**

The fabrication process of a SCOS occurs in three main steps and is pictured in Figure 2-6 [10]. First, the fiber jacket is removed and the fiber is cleaned using isopropyl alcohol. Second, the fiber is placed in a hydrofluoric acid etch to remove some of the cladding and exposing the evanescent field. Third, an electro-optic slab waveguide is glued to the fiber.

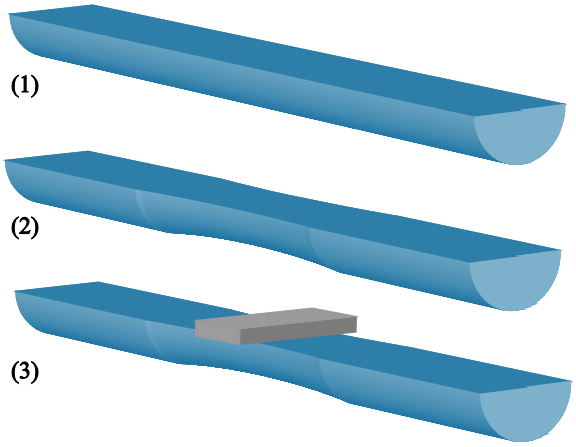

Figure 2-6: The SCOS fabrication process (1) The jacket is removed and the fiber is cleaned (2) the fiber is etched removing some of the cladding and exposing the evanescent field (3) An electro-optic slab waveguide is glued to the fiber

In order for the SCOS sensor to function, the electro-optic slab waveguide needs to be glued in close proximity to the core of the fiber. Figure 2-7 [23] shows the position of the core of the fiber. The D-shape of the fiber causes the core of the fiber to be close to the flat surface. Although the core is already close to the surface of the fiber, cladding still needs to be removed to allow coupling to occur.

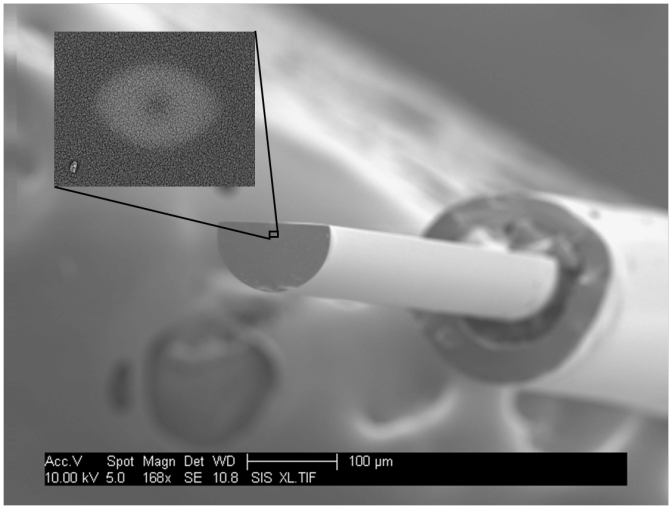

Figure 2-7: A 125 µm D-fiber with the elliptical core positioned 13 µm from the flat edge

A portion of the cladding is removed with a hydrofluoric acid etch. Figure 2-8 shows the setup for etching the fiber. To etch the fiber a two centimeter section of the fiber is stripped of the protective jacket exposing the bare fiber. The fiber is placed in an etch boat with two clamps holding the flat side of the fiber up with the stripped section in the middle. Sliding the clamps together causes the fiber to lower resulting in the stripped section entering the acid. Since the core of the fiber is about 13 μm to the surface of the D-shaped fiber removing 12 μm of the fiber cladding exposes the evanescent field without damaging the structural integrity of the fiber.

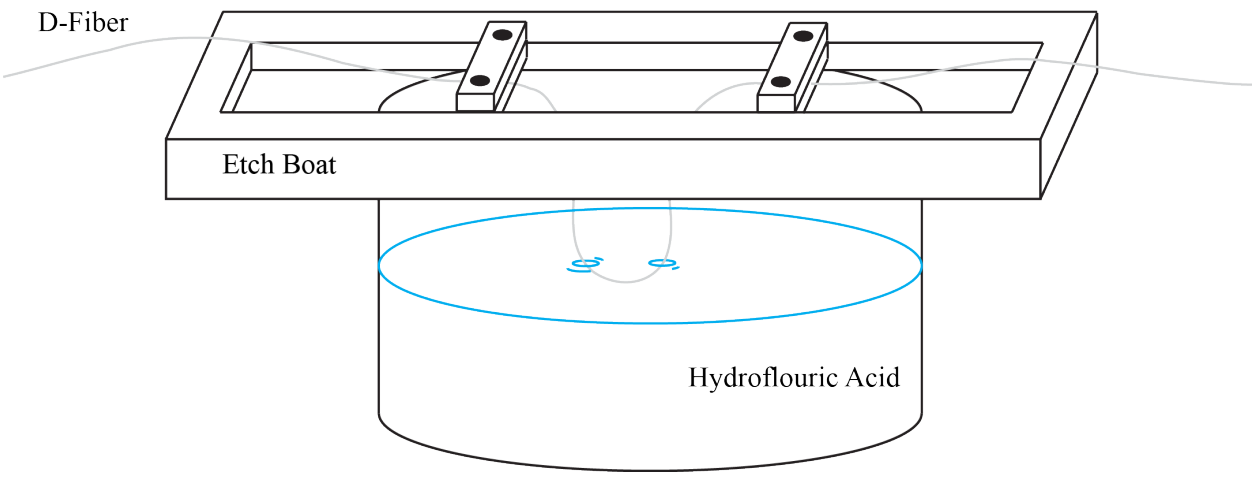

Figure 2-8: Setup for etching a D-fiber to remove cladding around the core.

The exposed evanescent field allows coupling between light in the fiber and a waveguide attached to the top of the waveguide. The coupling strength, κ, between the two waveguides is controlled by the separation distance between the slab waveguide and the core of the D-fiber [24]. The separation distance is dependent upon the depth of the etch and the location of the slab waveguide on the etched region. Figure 2-9 shows a cross section of an etched D-fiber. Fiber does not etch uniformly when it is submerged in hydrofluoric acid. The center section etches the most and the etch depth tapers off at the sides of the etched region. During fabrication the

coupling strength between the slab waveguide and the D-fiber is adjusted by sliding the slab across the etched region and changing the separation distance.

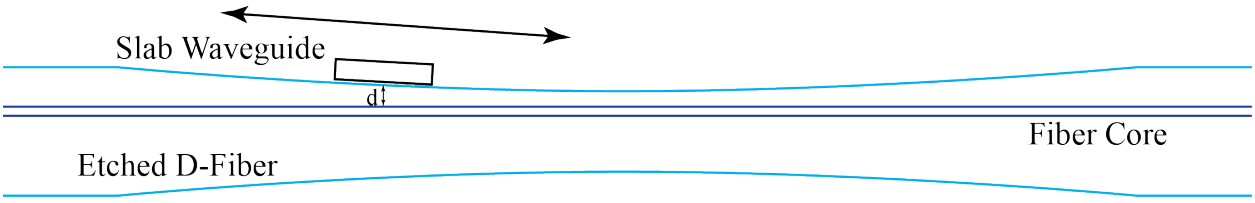

Figure 2-9: Sliding the slab waveguide along the transition region causes changes the coupling coefficient. Good coupling is achieved by moving the crystal across the transition region until the desired coupling is observed.

To insure coupling between the light traveling through the fiber and the slab waveguide, the transmission of the fiber is monitored on an optical spectrum analyzer as the slab is being attached. The slab is placed on the fiber with low index UV cure glue and gently pushed around the etched region until resonant dips are seen. For better sensitivity the slope of the resonance dip should be "steeper."

Figure 2-10 shows the transmission spectrum of a SCOS with the desired resonance dips. The "steep" slope is obtained by creating dips that are 15-20 dB deep. Resonance dips that are much less that 15 dB make the SCOS device less sensitive to electric fields and less valuable as a sensor.

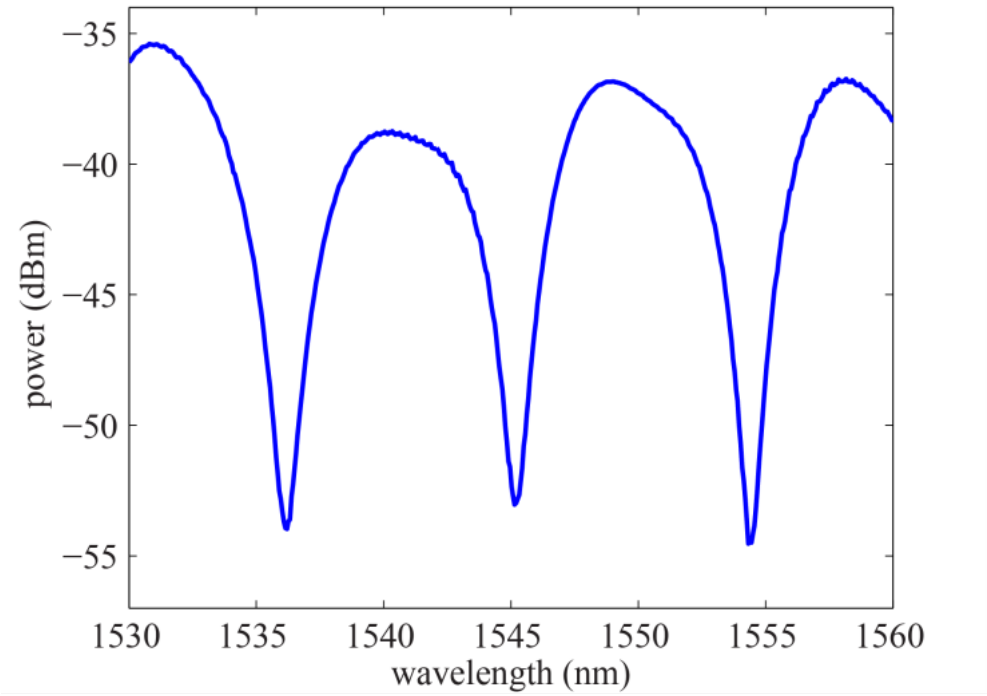

Figure 2-10: The transmission spectrum for a well-made SCOS. The resonance dips should be between 15 and 20 dB deep.

3 OFF AXIS SENSITIVITY

Three-axis electric field measurement requires three sensing elements that are only sensitive to a single direction. Sensitivity in the off-axis direction creates ambiguity in the measurement. This section discusses the directional sensitivity of the SCOS and determines the off-axis sensitivity.

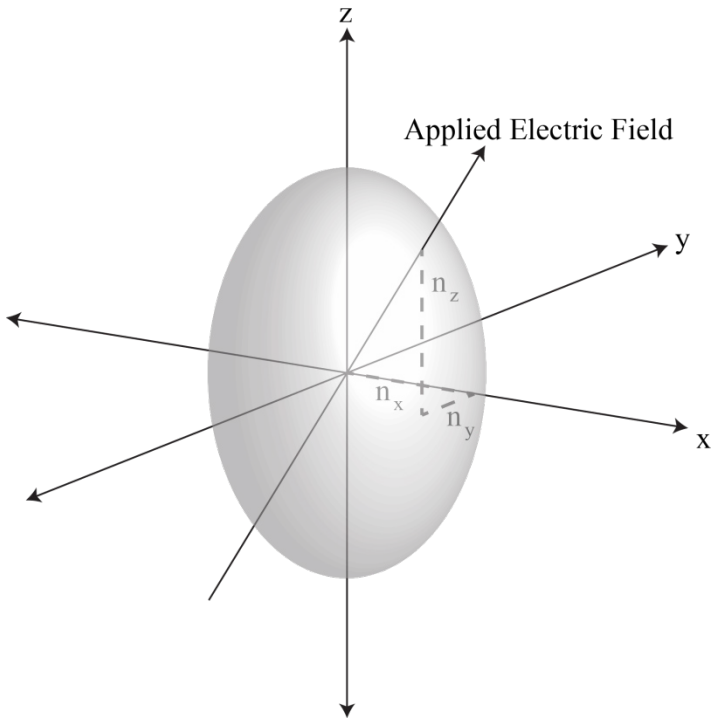

Figure 3-1: The index ellipsoid. The values for n_x, n_y, and n_z are determined by the direction the electric field is penetrating the ellipsoid.

Materials react differently to electric fields based on the material's crystal structure and is expressed using the index ellipsoid of the material. The sensitivity of a material to an electric field in an arbitrary direction is determined from the index ellipsoid of the material. Figure 3-1 shows the index ellipsoid which, for a birefringent crystal, can be represented in the form

$$\frac{x^2}{n_x^2} + \frac{y^2}{n_y^2} + \frac{z^2}{n_z^2} = 1, \tag{3-1}$$

where n_x, n_y, and n_z are the axis of the index ellipsoid. The values for n_x, n_y, and n_z are determined by the direction an electric field penetrates the ellipsoid.

Inserting the crystal into an electric field causes the orientation of the index ellipsoid to rotate. The equation for the rotated ellipsoid is

$$Ax^2 + By^2 + Cz^2 + Dyz + Exz + Fxy = 1, \tag{3-2}$$

where

$$\begin{aligned} A &= \frac{1}{n_x^2} + \Delta n_1, \\ B &= \frac{1}{n_y^2} + \Delta n_2, \\ C &= \frac{1}{n_z^2} + \Delta n_3, \\ D &= \Delta n_4, \\ E &= \Delta n_5, \\ F &= \Delta n_6. \end{aligned} \tag{3-3}$$

The Δn terms are solved for using the electro-optic tensor of the material and the components of the electric field penetrating the material and is given by

$$\begin{bmatrix} \Delta n_1 \\ \Delta n_2 \\ \Delta n_3 \\ \Delta n_4 \\ \Delta n_5 \\ \Delta n_6 \end{bmatrix} = \begin{bmatrix} r_{11} & r_{12} & r_{13} \\ r_{21} & r_{22} & r_{23} \\ r_{31} & r_{32} & r_{33} \\ r_{41} & r_{42} & r_{43} \\ r_{51} & r_{52} & r_{53} \\ r_{61} & r_{62} & r_{63} \end{bmatrix} \begin{bmatrix} E_x \\ E_y \\ E_z \end{bmatrix}, \tag{3-4}$$

where the r-tensor is the electro-optic tensor for the material and the E-vector contains the components of the electric field in the global x, y, and z directions. Equation (3-4) shows how the index of refraction is proportional to the direction of the electric field.

To completely eliminate off axis sensitivity the first two columns of the electro-optic tensor need to be zero. When this happens the only field that causes a change in refractive index is E_z. Unfortunately, there are no materials that contain only zeros in the first two columns. To eliminate a majority off axis sensitivity the r_{11}, r_{21}, r_{31}, r_{12}, r_{22}, and r_{32} terms need to be zero. This eliminates direct coupling between major axes and only allows for a rotation of the index ellipsoid.

Requiring these terms to be zero prohibits the use of crystals with trigonal crystal symmetry, such as lithium niobate and lithium tantalate, from being used in a multi-axis sensor. Materials that do have the required zeros to eliminate a majority of off-axis sensitivity are potassium titanyl phosphate (KTP) (orthorhombic crystal symmetry) and electro-optic polymer [25]. However, these materials still exhibit off-axis sensitivity to Δn_4, Δn_5, and Δn_6, which is discussed in subsections.

3.1 **Potassium Titanyl Phosphate (KTP) Sensitivity Analysis**

The electro-optic tensor for KTP is

$$r_{ij} = \begin{bmatrix} 0 & 0 & r_{13} \\ 0 & 0 & r_{23} \\ 0 & 0 & r_{33} \\ 0 & r_{42} & 0 \\ r_{51} & 0 & 0 \\ 0 & 0 & 0 \end{bmatrix} = \begin{bmatrix} 0 & 0 & 8.80 \\ 0 & 0 & 13.8 \\ 0 & 0 & 35.0 \\ 0 & 8.80 & 0 \\ 6.90 & 0 & 0 \\ 0 & 0 & 0 \end{bmatrix}. \tag{3-5}$$

Using the electro-optic tensor, the equation for the index ellipsoid is determined. The electro-optic tensor for KTP is substituted into Equation (3-4) yielding

$$\begin{aligned} \Delta n_1 &= r_{13}E_z, \\ \Delta n_2 &= r_{23}E_z, \\ \Delta n_3 &= r_{33}E_z, \\ \Delta n_4 &= r_{42}E_y, \\ \Delta n_5 &= r_{51}E_x, \\ \Delta n_6 &= 0. \end{aligned} \tag{3-6}$$

The Δn terms are substituted into Equation (3-3) and the resulting letters are substituted into Equation (3-2) yielding an index ellipsoid of form

$$\left(\frac{1}{n_x^2} + r_{13}E_z\right)x^2 + \left(\frac{1}{n_y^2} + r_{23}E_z\right)y^2 + \left(\frac{1}{n_z^2} + r_{33}E_z\right)z^2 + r_{42}E_y yz + r_{51}E_x xz = 1. \tag{3-7}$$

The cross terms resulting from r_{42} and r_{51} cause a rotation of the index ellipsoid resulting in crosstalk. In order to quantitatively determine the sensitivity, the change in each of the three indices (n_x, n_y, and n_z) is calculated with an electric field applied in the z direction. This change in the refractive index is divided by the corresponding refractive index change with the same electric field amplitude applied in the x and y directions.

3.1.1 Index Change From E = E_z

When the electric field is entirely in the E_z direction the E_x and E_y terms are zero and Equation (3-7) becomes

$$\left(\frac{1}{n_x^2}+r_{13}E_z\right)x^2+\left(\frac{1}{n_y^2}+r_{23}E_z\right)y^2+\left(\frac{1}{n_z^2}+r_{33}E_z\right)z^2=1. \tag{3-8}$$

In this case there are no cross terms and consequently no rotation about any of the axes. The new refractive indices become

$$\begin{aligned}\frac{1}{n_{x'}^2}&=\frac{1}{n_x^2}+r_{13}E_z,\\ \frac{1}{n_{y'}^2}&=\frac{1}{n_y^2}+r_{23}E_z,\\ \frac{1}{n_{z'}^2}&=\frac{1}{n_z^2}+r_{33}E_z.\end{aligned} \tag{3-9}$$

Solving for the new refractive indices yields

$$\begin{aligned}n_{x'}&=\left(\frac{1}{n_x^2}+r_{13}E_z\right)^{-\frac{1}{2}},\\ n_{y'}&=\left(\frac{1}{n_y^2}+r_{23}E_z\right)^{-\frac{1}{2}},\\ n_{z'}&=\left(\frac{1}{n_z^2}+r_{33}E_z\right)^{-\frac{1}{2}}.\end{aligned} \tag{3-10}$$

Using the approximation $(1-\varepsilon)^x=1-\varepsilon x$ when $\varepsilon \ll 1$ Equation (3-10) becomes

$$\begin{aligned}n_{x'}&=n_x-\frac{n_x^3}{2}r_{13}E_z,\\ n_{y'}&=n_y-\frac{n_y^3}{2}r_{23}E_z,\\ n_{z'}&=n_y-\frac{n_z^3}{2}r_{33}E_z.\end{aligned} \tag{3-11}$$

3.1.2 Index Change From E = E_y

When the electric field is entirely in the y-direction, Equation (3-7) becomes

$$\left(\frac{1}{n_x^2}\right)x^2 + \left(\frac{1}{n_y^2}\right)y^2 + \left(\frac{1}{n_z^2}\right)z^2 + 2r_{42}E_y yz = 1, \tag{3-12}$$

or

$$Ax^2 + By^2 + Cz^2 + DE_y yz = 1. \tag{3-13}$$

In this case there is a cross term causing a rotation of the index ellipsoid. Figure 3-2 shows a cross section of the rotated ellipsoid. In order to determine the effect of the rotation, the ellipsoid is rotated to get it into standard form and then solving as if there are no cross terms.

The ellipsoid after rotation about the x-axis is expressed as

$$A'x_1^2 + B'y_1^2 + C'z_1^2 + D'E_y y_1 z_1 = 1. \tag{3-14}$$

Rotating about the x-axis is done using the rotation equations

$$\begin{aligned} x &= x_1, \\ y &= y_1 \cos\theta_x - z_1 \sin\theta_x, \\ z &= y_1 \sin\theta_x + z_1 \cos\theta_x, \end{aligned} \tag{3-15}$$

where θ_x is the angle that the ellipsoid is rotated to get the ellipsoid into standard form.

The coefficients of the rotated index ellipsoid are determined by collecting all of the coefficients of the terms ${x_1}^2$, ${y_1}^2$, ${z_1}^2$, and $y_1 z_1$ and setting them equal to *A'*, *B'*, *C'*, and *D'* respectively and are expressed as

$$\begin{aligned} A' &= A, \\ B' &= B\cos^2\theta_x + C\sin^2\theta_x + D\sin\theta_x\cos\theta_x, \\ C' &= B\sin^2\theta_x + C\cos^2\theta_x - D\sin\theta_x\cos\theta_x, \\ D' &= -2B\sin\theta_x + 2C\sin\theta_x\cos\theta_x + D(\cos^2\theta_x - \sin^2\theta_x). \end{aligned} \tag{3-17}$$

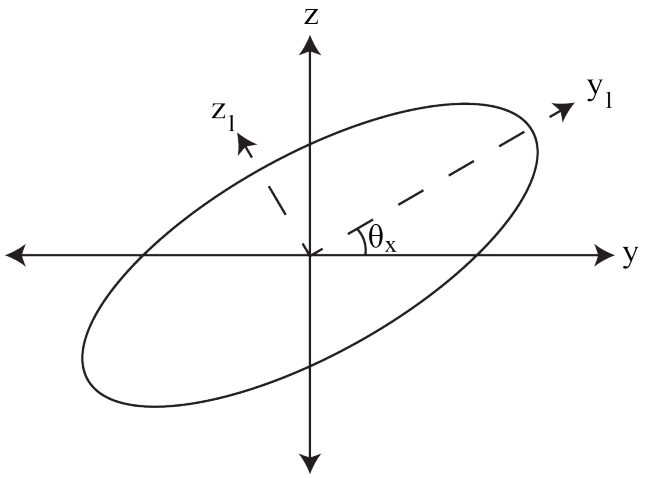

Figure 3-2: A cross section of the rotated index ellipsoid with the x axis out of the page.

By setting *D'* to zero and solving for θ_x, the magnitude of rotation is determined and consequently the effect of the applied electric field is also determined. Solving for θ_x yields

$$\theta_x = \frac{1}{2} tan^{-1}\left(\frac{D}{B-C}\right) = \frac{1}{2} tan^{-1}\left(\frac{2r_{42}E_y}{\frac{1}{n_y^2}-\frac{1}{n_z^2}}\right). \tag{3-18}$$

The value of θ_x is then substituted into (3-15) and values the coefficients of the rotated index ellipsoid, *A'*, *B'*, and *C'* are obtained. These values are then used to determine the resulting indices of refraction of the ellipsoid and are given by

$$n_{x'} = \sqrt{\frac{1}{A'}} = n_x,$$

$$n_{y'} = \sqrt{\frac{1}{B'}} = \sqrt{\frac{1}{\frac{1}{n_y^2}cos^2\theta_x + \frac{1}{n_z^2}sin^2\theta_x + 2r_{42}E_y sin\theta_x cos\theta_x}}, \tag{3-19}$$

$$n_{z'} = \sqrt{\frac{1}{C'}} = \sqrt{\frac{1}{\frac{1}{n_y^2}cos^2\theta_x + \frac{1}{n_z^2}sin^2\theta_x - 2r_{42}E_y sin\theta_x cos\theta_x}}.$$

3.1.3 Index Change From E = E_x

When the electric field is entirely in the x-direction, (3-7) becomes

$$\left(\frac{1}{n_x^2}\right)x^2 + \left(\frac{1}{n_y^2}\right)y^2 + \left(\frac{1}{n_z^2}\right)z^2 + 2r_{51}E_x xz = 1, \tag{3-20}$$

or

$$Ax^2 + By^2 + Cz^2 + 2FE_x xz = 1. \tag{3-21}$$

Again, this equation needs to be rotated to determine the new refractive indices due to the x-direction electric field. Figure 3-3 shows a cross section of the index ellipsoid and the angle θ_y that the ellipsoid needs to be rotated. The new rotation equations are

$$\begin{aligned} x &= x_2 \cos\theta_y - z_2 \sin\theta_y, \\ y &= y_2, \\ z &= x_2 \sin\theta_y + z_2 \cos\theta_y. \end{aligned} \tag{3-22}$$

To solve for θ_y the same process is used as was used for the y-direction electric field. The coefficients of the rotated index ellipsoid become

$$\begin{aligned} A' &= A\cos^2\theta_y + C\sin^2\theta_y + F\sin\theta_y\cos\theta_y, \\ B' &= B, \\ C' &= A\cos^2\theta_y + C\sin^2\theta_y - F\sin\theta_y\cos\theta_y, \\ F' &= -2A\sin\theta_y + 2C\sin\theta_y\cos\theta_y + F\left(\cos^2\theta_y - \sin^2\theta_y\right). \end{aligned} \tag{3-23}$$

Setting *F'* equal to zero and solving for θ_y yields

$$\theta_y = \frac{1}{2}\tan^{-1}\left(\frac{F}{A-C}\right) = \frac{1}{2}\tan^{-1}\left(\frac{2r_{51}E_x}{\frac{1}{n_x^2} - \frac{1}{n_z^2}}\right). \tag{3-24}$$

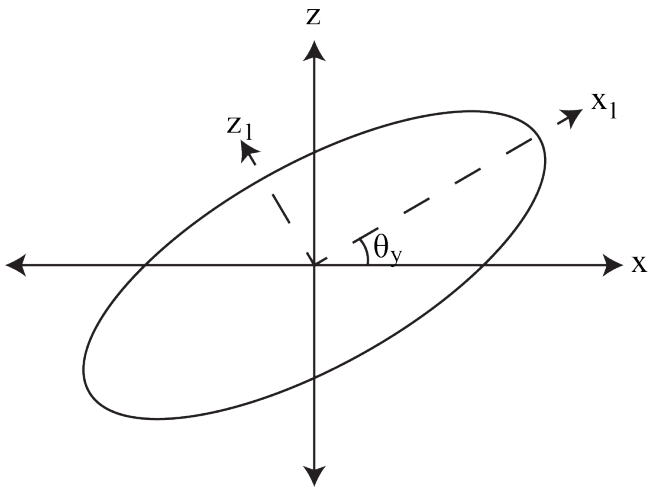

Figure 3-3: A cross section of the rotated index ellipsoid with the y axis into the page.

Substituting the value for θ_y into Equation (3-23) provides the values for *A'*, *B'*, and *C'* which are used to determine the new refractive indices. The actual values of the shifted refractive indices are solved for using

$$n_{x'} = \sqrt{\frac{1}{A'}} = \sqrt{\frac{1}{\frac{1}{n_x^2}cos^2\theta_y + \frac{1}{n_z^2}sin^2\theta_y + 2r_{51}E_x sin\theta_y cos\theta_y}},$$

$$n_{y'} = \sqrt{\frac{1}{B'}} = n_y, \tag{3-25}$$

$$n_{z'} = \sqrt{\frac{1}{C'}} = \sqrt{\frac{1}{\frac{1}{n_x^2}cos^2\theta_y + \frac{1}{n_z^2}sin^2\theta_y - 2r_{51}E_x sin\theta_y cos\theta_y}}.$$

3.1.4 KTP Off-Axis Sensitivity

In order to quantitatively determine the sensitivity, the change in each of the three indices (n_x, n_y, and n_z) from a field applied in the z direction is divided by the corresponding refractive

index change with the same electric field amplitude applied in the x and y directions. The resulting index ratios are given by

$$\Delta n_{ij} = \frac{n_i(E_z = E_0) - n_i}{n_i(E_j = E_0) - n_i}, \tag{3-26}$$

where *i* signifies the three possible refractive index components (*i*=*x*,*y*,*z*) and *j* signifies the off-axis electric field component (*j*=*x*,*y*). This ratio is plotted in Figure 3-4 with a varying electric field and initial KTP index values of

$$\begin{aligned} n_x &= 1.7295, \\ n_y &= 1.7349, \\ n_z &= 1.8158. \end{aligned} \tag{3-27}$$

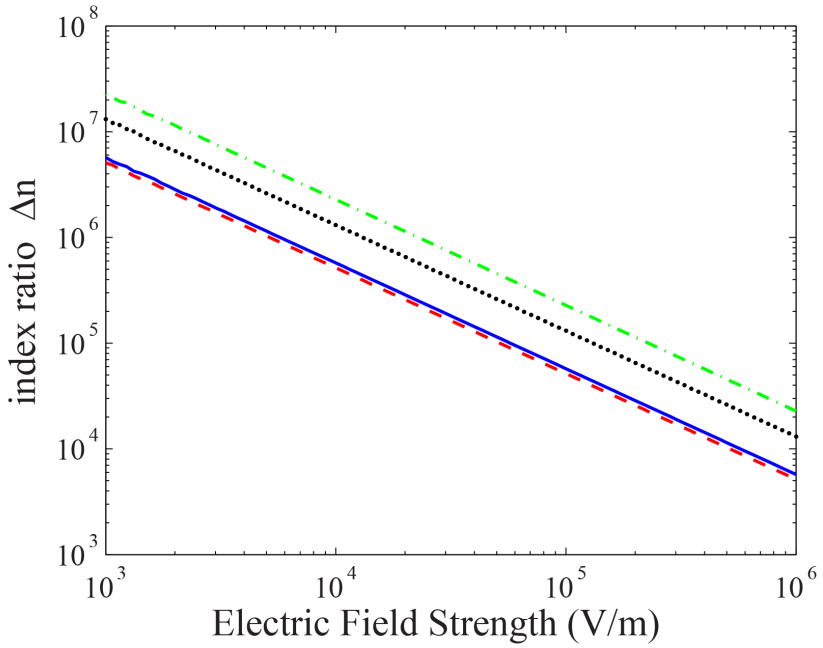

Figure 3-4: Ratio of refractive index change in KTP due to different electric fields. The dash-dot line is the ratio Δn_{zx}, the dotted line is the ratio Δn_{zy}, the solid line is the ratio Δn_{xx}, and the dashed line the ratio Δn_{yy}.

Figure 3-4 shows that the influence of the cross terms increases as the strength of the electric field gets larger. In a strong electric field of 100 kV/m the ratio between the induced index shifts from a z-directional field is 47 dB more than the induced index shift from either an x or a y directional field. Therefore, the off-axis sensitivity for KTP can be neglected without any significant change in the measurement.

3.2 **Analysis of Electro-optic Polymer**

Electro-optic polymer is also a good waveguide for use in SCOS devices. The amount of off axis sensitivity it exhibits can be determined in the same manner KTP. The only difference in the analysis is the electro-optic tensor of KTP is replaced with the electro-optic tensor of polymer. The electro-optic tensor for polymer is

$$r_{ij} = \begin{bmatrix} 0 & 0 & 23 \\ 0 & 0 & 23 \\ 0 & 0 & 70 \\ 0 & 23 & 0 \\ 23 & 0 & 0 \\ 0 & 0 & 0 \end{bmatrix}. \tag{3-28}$$

3.2.1 **Polymer Off Axis Sensitivity**

For polymer the initial indices of refraction are

$$\begin{aligned} n_x &= 1.66, \\ n_y &= 1.66, \\ n_z &= 1.74, \end{aligned} \tag{3-29}$$

which are used in conjunction with the electro-optic tensor for polymer to determine the change in refractive indices due to an applied electric field.

Again the change due to an applied z-direction electric field is much greater than the change due to either the x-direction of y-direction electric fields. The ratio between the induced change from a z-direction electric field and the induced change from fields in other directions shows that polymer is much more sensitive to the z-field. These ratios are shown in Figure 3-5.

The analysis of electro-optic polymer shows that the change in refractive index from a z direction electric field is 41 dB more than the change induced by electric fields in the x or the y directions. Because a z direction electric field causes much larger changes in the refractive index in both KTP and electro-optic polymer than electric fields in other directions, the amount of crosstalk they exhibit is negligible making both KTP and polymer good options for multi-axis sensing.

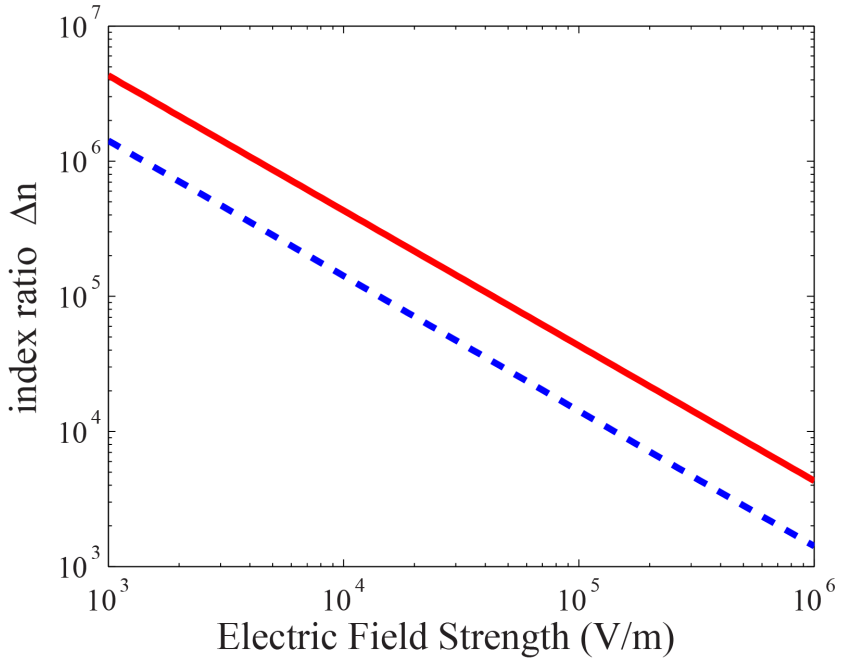

Figure 3-5: Ratio of refractive index change in Polymer due to different electric fields. The solid line is the ratios Δn_{xx} and Δn_{yy}. The dashed line is the ratios Δn_{zx} and Δn_{zy}.

The crystal structures of KTP and electro optic polymer make them insensitive to electric fields that are not parallel to their optic axis. When used in a SCOS device, the device is only sensitive to electric fields parallel to the optic axis of the material allowing the sensor to be used in conjunction with two other sensors to entirely map an electric field.

4 MULTI-AXIS SCOS

A single SCOS device can be used to detect the magnitude of an electric field in the direction of its optic axis but cannot determine the direction of an arbitrary electric field. In order to determine the direction of an electric field, three sensors must be used in conjunction with each sensor detecting a portion of the electric field. Every electric field can be broken down into three component fields in the axial directions. Each of the SCOS devices detects one of the three electric field components. The signals from the three devices are then used to determine the direction of the electric field relative to the SCOS device.

4.1 Mapping Method

The directional sensitivity of both KTP and electro-optic polymer causes the SCOS to only be sensitive to the component of the electric field parallel to the z-axis or optic axis of the crystal. Each of the three SCOS detects a portion of the signal which is then mapped to the overall electric field.

The mapping method uses four different coordinate systems. Each SCOS has its individual coordinate system that is dictated by the crystal structure and the electric field is defined using a global coordinate system. Figure 4-1 shows the various coordinate systems.

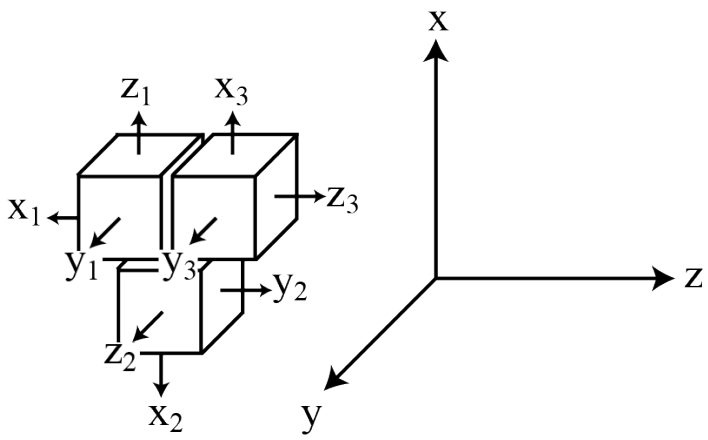

Figure 4-1: Four coordinate systems for the multi-axis SCOS.

If each individual SCOS coordinate system were perfectly aligned to one of the global coordinate system axes then the mapping is simple. As an example, the mapping for Figure 4-1 would be $E_x = \frac{V_1}{C_1}$, $E_y = \frac{V_2}{C_2}$, and $E_z = \frac{V_3}{C_3}$, where V_i is the measured voltage and C_i is the calibration factor for the i^{th} SCOS.

In practice the optic axis of each SCOS is in a different direction than the global coordinate axes and often the sensors will not be totally orthogonal to each other. In order to accommodate this discrepancy, each of the three optic axes (z_1, z_2, and z_3) is defined by a unit vector using the global coordinate system.

When the x global axis is used as the reference vector then the unit vector for the first SCOS is defined as

$$\widehat{s_1} = 1\hat{x} + 0\hat{y} + 0\hat{z}, \tag{4-1}$$

where $\hat{x}$, $\hat{y}$, and $\hat{z}$, are the unit vectors in the global coordinate directions. Figure 4-2 shows that the global coordinate system can be configured such that the unit vector for both the first and second SCOS both lie within the xy plane resulting in

$$\hat{s_2} = s_{2x}\,\hat{x} + s_{2y}\,\hat{y} + 0\hat{z}\,, \tag{4-2}$$

where $\sqrt{s_{2x}^2 + s_{2y}^2} = 1$. Figure 4-2 also shows that the final unit vector can have components in all three direction and is given by

$$\hat{s_3} = s_{3x}\,\hat{x} + s_{3y}\,\hat{y} + s_{3z}\hat{z}. \tag{4-3}$$

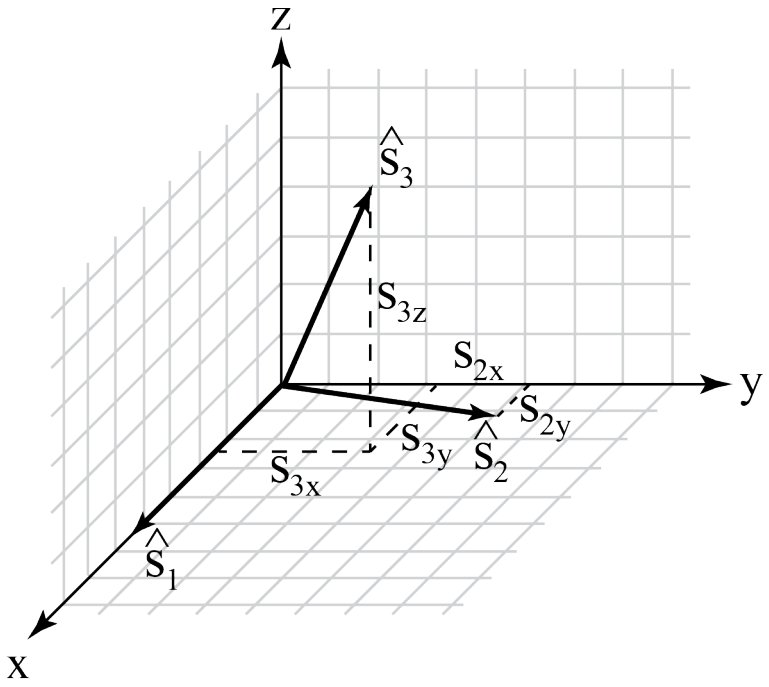

Figure 4-2: Unit vectors for the three optic axes relative to the global axes.

The unit vectors in combination with the calibration factors are used to create a sensitivity matrix that is used to solve for the vector representing the electric field as given by

$$\begin{bmatrix} C_1 & 0 & 0 \\ C_2 s_{2x} & C_2 s_{2y} & 0 \\ C_3 s_{3x} & C_3 s_{3y} & C_3 s_{3z} \end{bmatrix} \begin{bmatrix} E_x \\ E_y \\ E_z \end{bmatrix} = \begin{bmatrix} V_1 \\ V_2 \\ V_3 \end{bmatrix}, \tag{4-4}$$

where V_1, V_2, and V_3 are measured signals, C_1, C_2, and C_3 are the calibration factors, and E_x, E_y, and E_z are the estimated electric field components.

4.2 **Packaging**

The requirements for the packaging of a three-axis SCOS sensor are (1) the sensor needs to be protected, (2) each sensor needs to be packaged separately, and (3) the packaging needs to be able to be attached to each other at right angles. Etched D-fiber is fragile and even small amounts of handing can cause the fiber to break. Packaging protects the fiber allowing the SCOS device to be handled with less change of breaking. Separate packaging allows each SCOS device to be packaged immediately after it is fabricated lowering the chance of breaking and also allows a single sensor to be replaced if it stops functioning correctly. Right angle packaging lets the sensors be mounted orthogonally to each other helping in fabrication of a multi-axis sensor.

To fulfill these needs small troughs were created out of FR4 board and Plexiglas that the sensor can be inserted into and then covered with low index epoxy to protect the SCOS [26]. Figure 4-3 shows a cross section of this packaging.

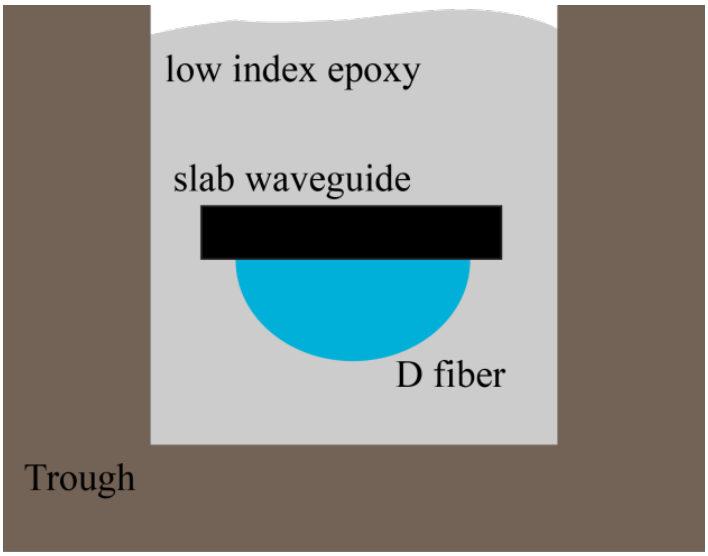

Figure 4-3: A cross section of a SCOS device in packaging

The SCOS device is surrounded on all sides to reinforce the structure and protect the weaker etched region of the fiber. Individual packaging allows single sensors to be replaced if an individual sensor is broken or goes bad. The flat sides allow multiple sensors to be glued together so that the three sensors can be attached orthogonally to each other.

To create a trough out of FR4 board a small piece (around 5 cm x 0.4 cm x 0.2 cm) is cut from a larger piece using a notching shear. The cut out piece is then placed in a mill and clamped in. The middle of the board is then milled out with a 1 mm thick mill bit creating a trough. Figure 4-4 shows a photograph of a milled FR4 board trough.

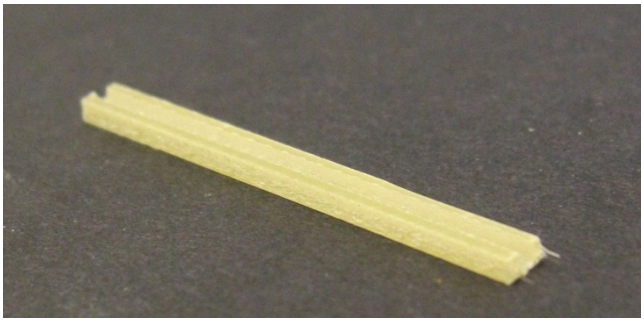

Figure 4-4: A photograph of a FR4 board trough.

FR4 board packaging keeps the height of the packaging small while maintaining a flat rigid structure. The disadvantage of FR4 board is that it is often difficult to clamp and mill a board of this size. If the two sides of the board are not parallel, the board is difficult to clamp in place and the trough down the middle will often be off center or diagonal.

Another option for SCOS packaging is using laser-cut Plexiglas. The Plexiglas is formed into a trough by placing a 3 mm thick Plexiglas sheet in the laser cutter. The laser cutter is programmed to cut out a trough of the desired size and shape. The settings for the laser cutter in the BYU electrical engineering shop are provided in Appendix A.

Figure 4-5 shows a photograph of a completed Plexiglas trough. Using Plexiglas for the trough is usually easier because the laser can be set to print without supervision. The ends of the trough can also be cut lower to add room for any tubing that is used to protect the bare fiber that extends outside of the trough. The disadvantages of Plexiglas are that the raw material is thicker leading to a larger package and the heat of the laser cutter often warps the Plexiglas preventing it from being entirely flat on the bottom.

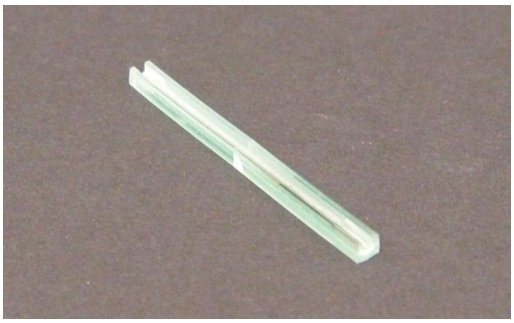

Figure 4-5: Photograph of a completed Plexiglas trough.

4.3 **Three Axis Sensor**

To increase the signal to noise ratio the optic axis of each electro-optic crystal needs to be approximately orthogonal to that of the other two. Figure 4-6 shows one configuration using three SCOS devices. In this configuration the electro-optic crystal has its optic axis normal to its surface and is called z-cut. Z-cut crystals cause the optical axes of the SCOS to always be normal to the flat surface of the D-fiber. Figure 4-6 shows that even though the sensing volume of this configuration can be small, it has a large planar packaging size because of the limited bend radius of the optical fiber [27]. The resulting packaging size is on the order of 40mm X 2mm X 40mm.

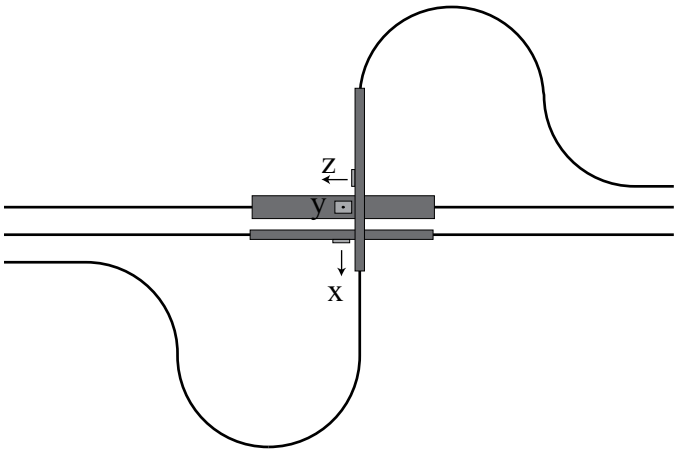

Figure 4-6: Setup for a 3-axis SCOS.

To reduce the size of the sensor, the slab waveguide that is sensitive to fields in the x direction is replaced with a slab waveguide that has its optic axis parallel to the direction of the fiber. Figure 4-7 shows that this is accomplished using x-cut KTP allowing all three fibers to be parallel to each other. X-cut KTP is polished so that the x-direction of the crystal is normal to the surface resulting in the optical axis (z-direction) being within the plane of the crystal. The x-cut crystal enables the optical axis of the SCOS to be aligned with the fiber propagation direction.

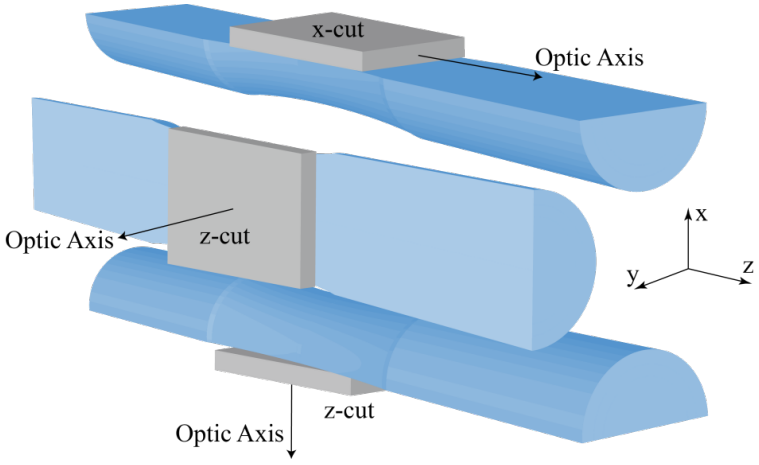

Figure 4-7: Setup of a 3-axis SCOS using x-cut KTP.

Figure 4-8 illustrates how two packaged SCOS are glued back to back with a third SCOS attached to the side of the other two resulting in a 3-axis SCOS device with nearly orthogonal optic axes. Using this setup, the sides of the packaging are aligned to each other making the error in alignment dependent upon the alignment of the SCOS to the individual packages.

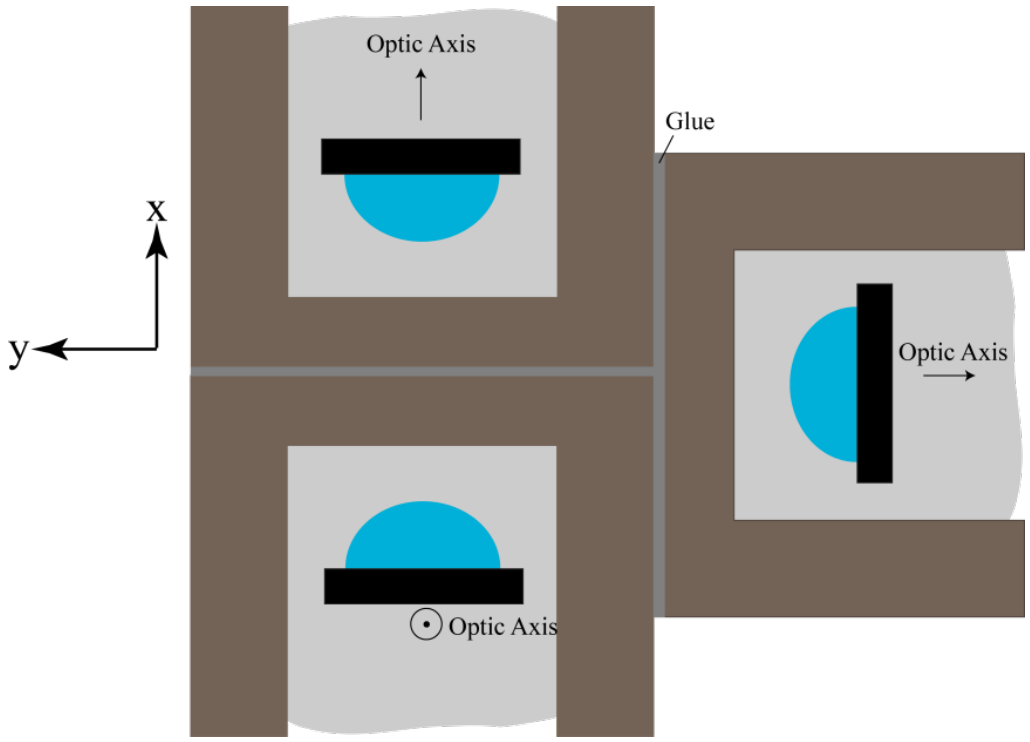

Figure 4-8: A cross sectional view of a 3-axis SCOS sensor.

A 3-axis SCOS device was fabricated using an x-cut KTP crystal, a z-cut KTP crystal, and an electro-optic polymer. The electro-optic polymer was used to demonstrate the ability to mix different sensing materials. Figure 4-9 shows a photograph of an actual 3-axis sensor using FR4 board packaging. The location of the three sensors in in the middle of each of the three FR4 board packages and the resulting size of this sensor is 70 mm x 6 mm x 4mm.

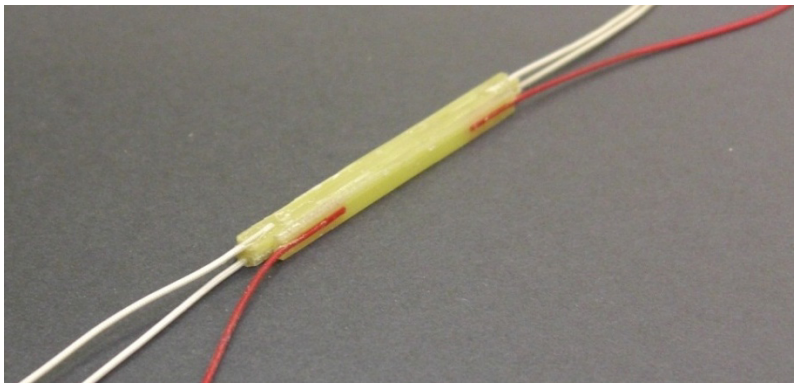

Figure 4-9: A photograph of a 3-axis SCOS sensor.

5 THREE AXIS SCOS MEASUREMENTS

To determine how well the sensor detects electric field direction it needs to be calibrated. To do this the sensors needs to be interrogated over a large range of angles and the accuracy of the sensor alignment needs to be determined.

5.1 Measurement Configuration

Figure 5-1 shows that the three axis SCOS is interrogated using three tunable lasers, three optical detectors, a three channel DC current block, three transimpedance amplifiers, and an oscilloscope. Each tunable laser is tuned to the wavelength that provides the largest signal-to-noise ratio (SNR) for the SCOS that it is connected to. The wavelength was deteremined by connecting the output of the transimpedance analyzer to an electrical spectrum analyzer and cycling through different wavelenths until the wavelength was found that provided the highest SNR.

The output of the optical detectors have a large DC optical power, which would overload the amplifier. Therefore, a DC current block is used prior to the transimpedance amplifiers. The resulting amplified signal is then recorded using the oscilloscope. Also pictured in Figure 5-1 are a function generator and a pair of electrodes that are used to generate a known electric field.

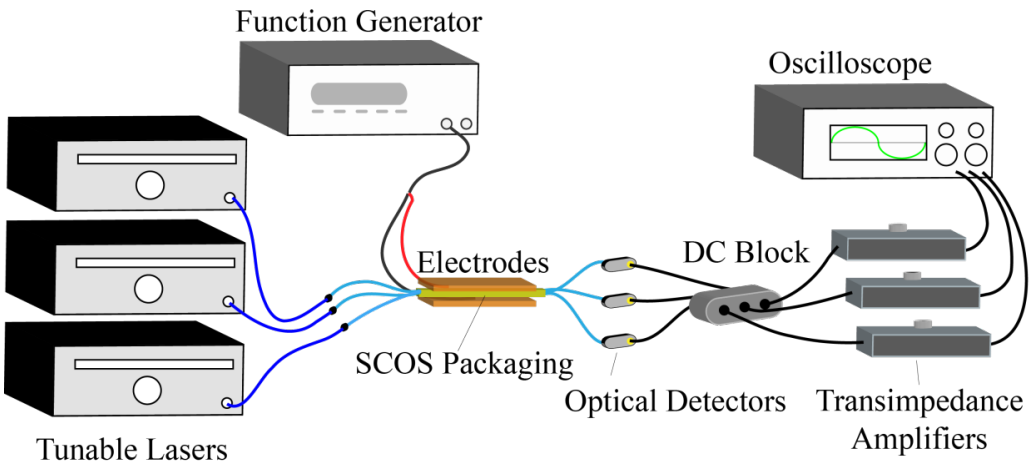

Figure 5-1: SCOS interrogation setup

Figure 5-2 illustrates how the electric field is applied by placing the SCOS sensor between two parallel electrodes. The electrodes are then rotated with one degree increments to change the direction of the electric field relative to the sensor. This configuration creates a known electric field with an angle that lies in the xy plane.

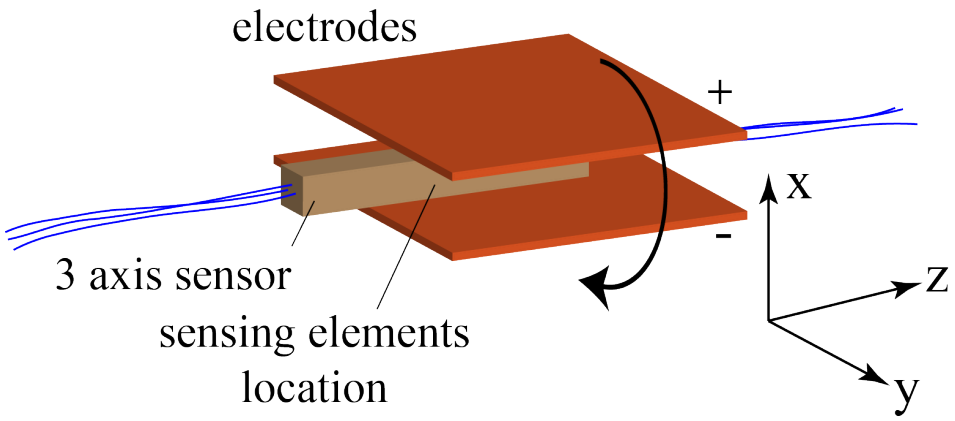

Figure 5-2: Setup to test xy applied electric field.

In order to characterize the multi-axis SCOS relative to the z-axis, Figure 5-3 shows how the experiment is repeated by placing the sensor next to the two electrodes. In this configuration the SCOS device detects the fringe field that is created by the two electrodes. Again the

electrodes are rotated at one degree increments changing the relative direction of the electric field. This configuration creates a known electric field with an angle that lies in the xz plane.

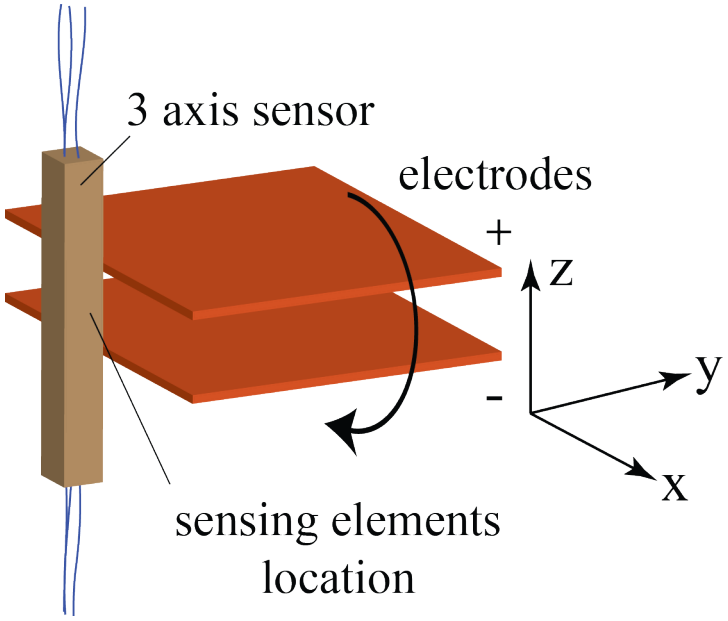

Figure 5-3: Setup to test xz applied electric field.

Figure 5-4 shows a picture of the test setup. In the center of the picture is the 3-axis SCOS which is held between the two copper electrodes. The electrodes are attached to a rotation stage that uniformly moves the electrodes around the SCOS changing the electric field.

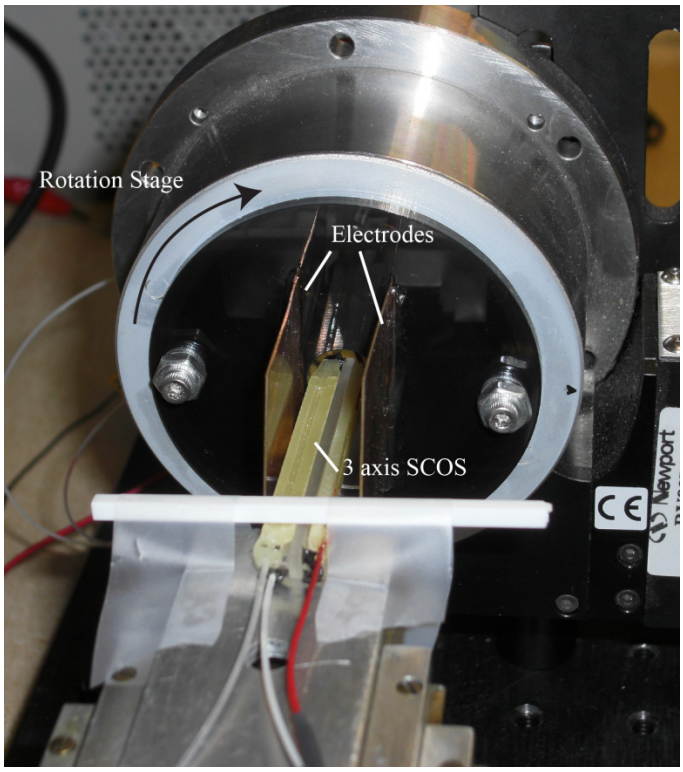

Figure 5-4: A photograph of the 3-axis SCOS device between two rotating electrodes.

5.2 Sensor Calibration

The sensor calibration includes determining (1) the optimum wavelength for each SCOS, (2) the unit vectors for each SCOS, and (3) the calibration factor for each SCOS. Figure 5-5 shows the measured resonance for each SCOS. The most sensitive wavelength for the SCOS device depends on the slope of the resonance, the shift as a function of the applied field, and the total power transmitted through the SCOS. The optimum wavelength was determined by applying a sinusoidal voltage to the electrodes and then stepping through the wavelengths until the greatest SNR was detected by the oscilloscope.

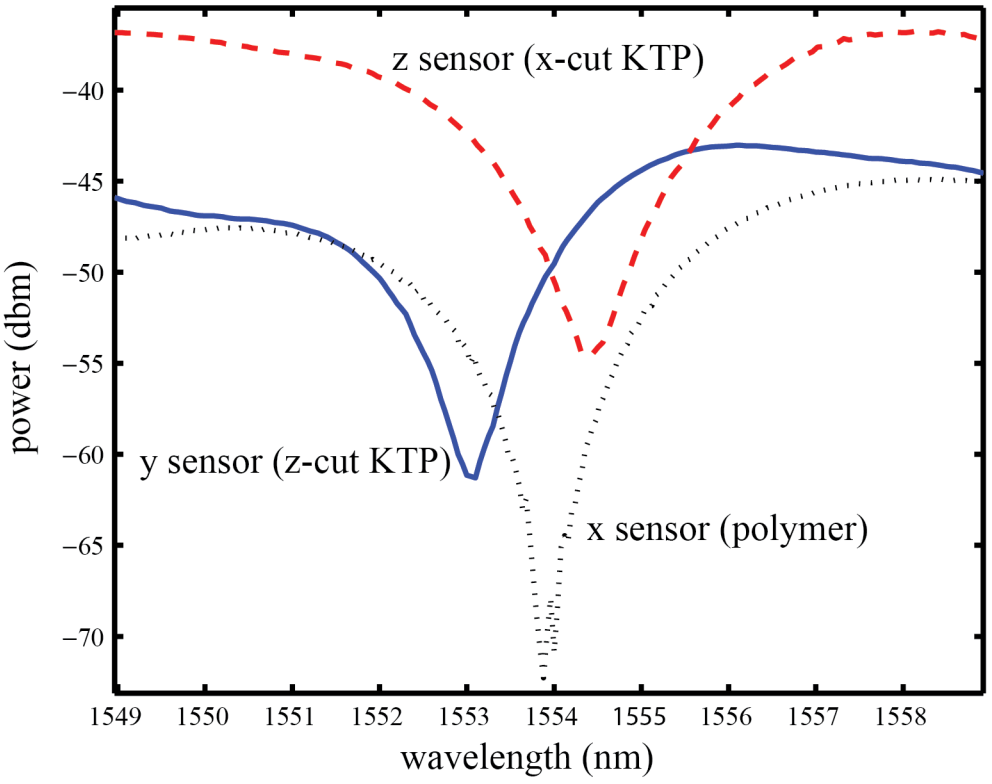

Figure 5-5: The resonance dips for the 3-axis SCOS that was used in testing. The x sensor used polymer, the y sensor was z-cut KTP, and the z sensor used x-cut KTP.

The unit vectors that correspond to the optic axis for the three electro-optic crystals ($\widehat{s_1}$, $\widehat{s_2}$, $\widehat{s_3}$) are determined by making three different angle measurements. Figure 5-4 shows the configuration used to make each of the angle measurements. In each of the measurements the multi-axis SCOS is aligned such that the rotation axis of the test set-up is parallel to one of the SCOS axes.

Figure 5-6 shows that in the first configuration $\widehat{s_3}$ is parallel to the rotation axis. Since the electric field is normal to the parallel plate electrodes, the electric field relative to the unit vectors is essentially rotated about the xy plane.

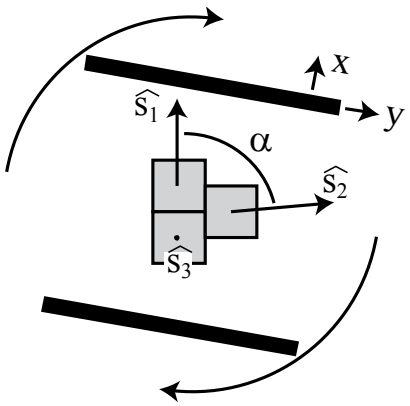

Figure 5-6: Illustration of the measurement configuration with the unit vector of the third SCOS aligned to be parallel to the rotation axis of the test set-up. The thick black lines correspond to the parallel plate electrodes.

The SCOS produces a maximum voltage when the electric field is aligned with the SCOS unit vector and a minimum when it is perpendicular. Therefore, by simultaneously measuring the normalized voltage for the first and second SCOS we can find the angular difference between their unit vectors (labeled as α in Figure 5-6) by simply finding the angular difference between the two maxima or finding the angle offset between the maximum of one and the minimum of the other. Figure 5-7 shows that the angles between the other unit vectors are found in a similar method but with the 3-axis SCOS placed in front of the electrode.

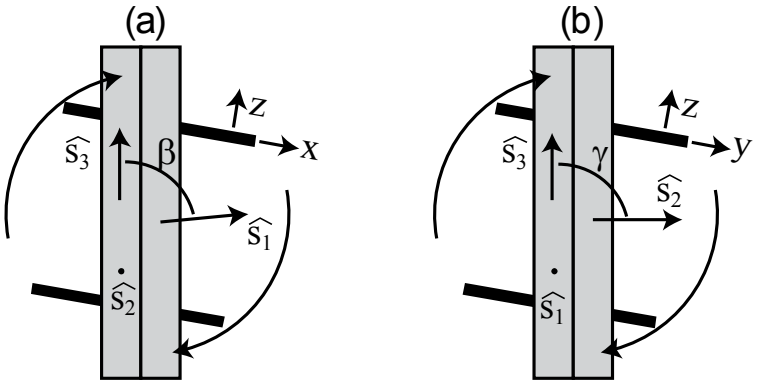

Figure 5-7: Illustration of the measurement configuration with the unit vector of the (a) second and (b) first SCOS aligned to be parallel to the rotation axis of the test set-up. The thick black lines correspond to the parallel plate electrodes.

The unit vectors are determined from the three angular measurements by using dot products between the unit vectors resulting in

$$\widehat{s_1} \cdot \widehat{s_2} = \cos\alpha\,, \tag{5-1}$$

$$\widehat{s_1} \cdot \widehat{s_3} = \cos\beta\text{, and} \tag{5-2}$$

$$\widehat{s_2} \cdot \widehat{s_3} = \cos\gamma\,. \tag{5-3}$$

Equations (5-1)-(5-3) can be combined with Equations (4-1)-(4-3) to yield

$$s_{2x} = \cos\alpha\,, \tag{5-4}$$

$$s_{2y} = \sqrt{1 - s_{2x}^2}, \tag{5-5}$$

$$s_{3x} = \cos\beta\,, \tag{5-6}$$

$$s_{3y} = \frac{\cos\gamma - s_{2x}s_{3x}}{s_{2y}}\text{, and} \tag{5-7}$$

$$s_{3z} = \sqrt{1 - s_{3x}^2 - s_{3y}^2}. \tag{5-8}$$

Figure 5-8 shows the normalized voltage measurements for SCOS 1 and 2 as a function of field angle. In this measurement the angle offset (the distance between a maximum and a minimum) is used because it requires a smaller range of measurement angle. In the sensor used the measured unit vector separation angles are α=87º and β=81º. The packaging method used resulted in γ being smaller than the resolution this test is able to detect so it is approximated with γ =90º.

In order to determine the calibration factor of each SCOS device, a voltage was applied to parallel plate electrodes with a known separation. The SCOS voltage is measured then filtered and the data is fit to a curve with form of $a_1\sin(b_1 t + c_1)$.

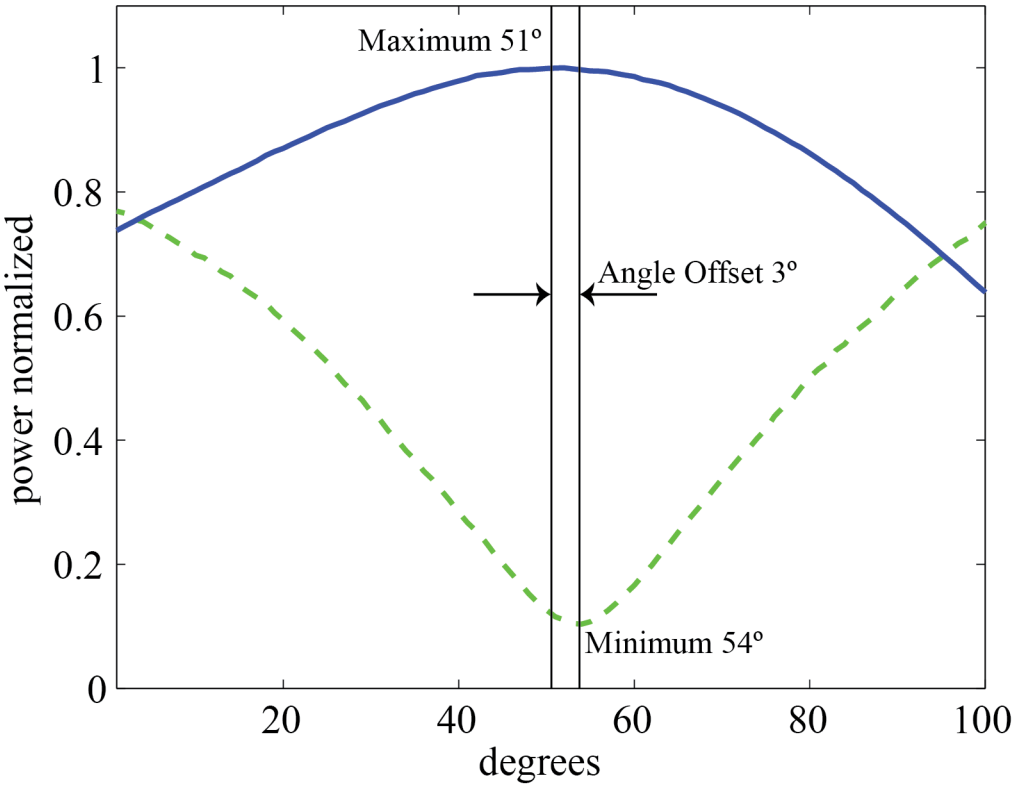

Figure 5-8: The normalized voltage as a function of angle for (solid) SCOS 1 and (dashed) SCOS 2. The difference between the maximum of sensor 1 and the minimum of sensor 2 is the angle offset.

The calibration factor is expressed as

$$C = \frac{a_1}{\left(\frac{V_e}{d}\right)}, \tag{5-9}$$

where V_e is the voltage applied to the electrodes and d is the spacing between the electrodes. Figure 5-9 shows the measured SCOS voltage along with the numerical fit. The fit for sensor 1 resulted in a_1=83 mV. This fit parameter in combination with the known electrode spacing of d=1.5cm and applied voltage of V_e=500 V results in a calibration factor of $C_1 = 2.5\frac{mV}{kV/m}$. The same process was also performed for the other two SCOS resulting in $C_2 = 0.12\frac{mV}{kV/m}$, and $C_3 = 0.84\frac{mV}{kV/m}$.

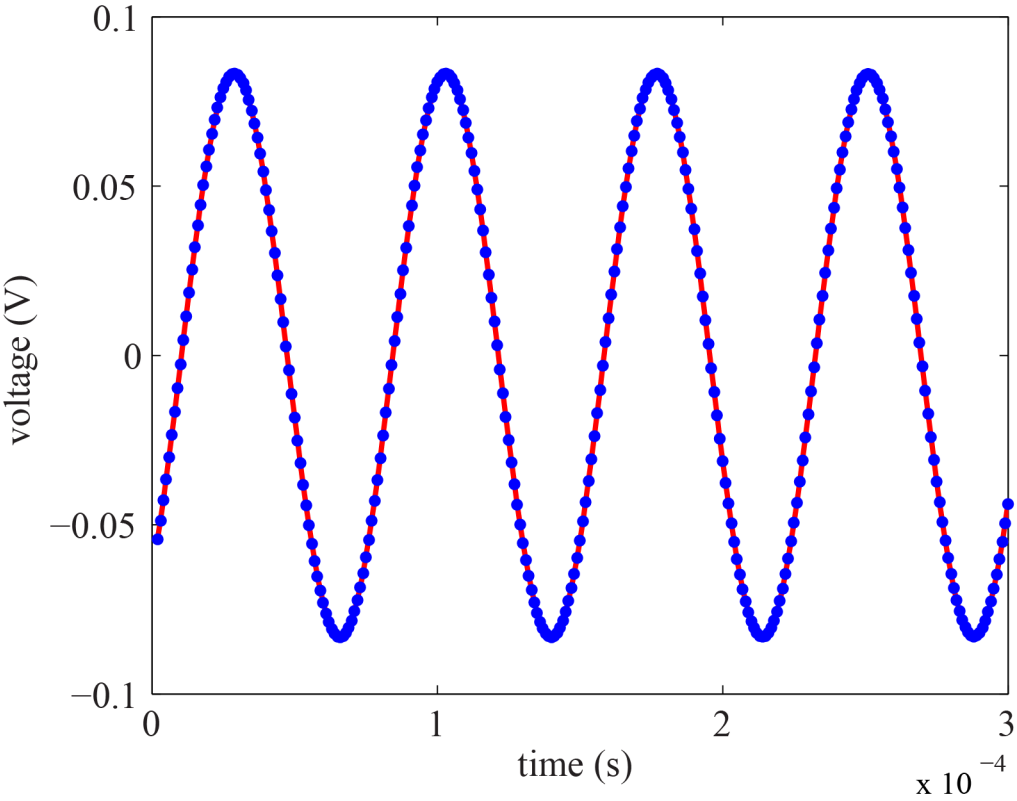

Figure 5-9: The measured voltage after filtering over sensor 1 (dotted line) with the best fit line (solid line).

The unit vectors for the three optic axes are obtained from α, β, and γ resulting in

$$\hat{s_1} = 1\hat{x} + 0\hat{y} + 0\hat{z}, \tag{5-10}$$

$$\hat{s_2} = 0.0525 + 0.988\hat{y} + 0\hat{z}, \text{ and} \tag{5-11}$$

$$\hat{s_3} = 0.156\hat{x} + 0\hat{y} + 0.988\hat{z}. \tag{5-12}$$

The unit vectors in combination with the calibration factors are used to form the sensitivity matrix which becomes

$$\begin{bmatrix} 2.5 & 0 & 0 \\ 0.0063 & 0.1198 & 0 \\ 0.1314 & 0 & 0.8297 \end{bmatrix} \begin{bmatrix} E_x \\ E_y \\ E_z \end{bmatrix} = \begin{bmatrix} V_1 \\ V_2 \\ V_3 \end{bmatrix}, \tag{5-13}$$

where the measured voltages are in units of mV and the electric field is in units of kV/m.

5.3 **Multi-Axis Accuracy**

The error for each of the two rotations are used determine how accurately the sensor predicts the direction of a three dimensional electric field. In each test the field was detected by two of the sensors and only noise was detected on the output of the third sensor. The tangent of the two vectors was taken to determine estimated field direction and compared to the angle of the actual field direction to determine the error in the angle. Figure 5-10a shows the error in the predicted angle for the xy field test (see Figure 5-2) and Figure 5-10b shows the error for the xz test (see Figure 5-3).

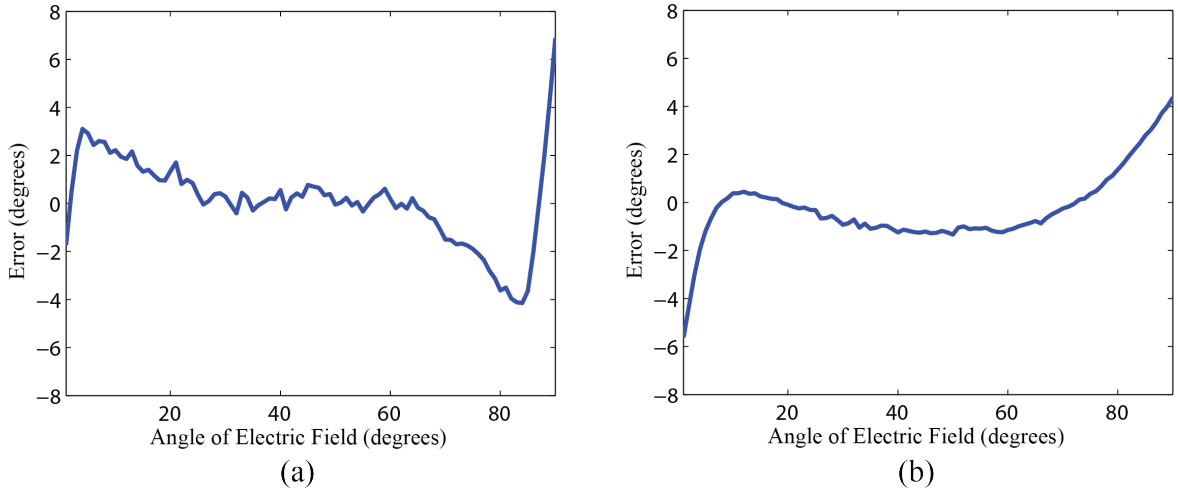

Figure 5-10: (a) Angle error with the electric field applied in the xy plane. (b) Angle error with the electric field applied in the xz plane.

For the xy test the average absolute error is 1.26º with a standard deviation of 1.82º. For the xz test the average absolute error was 1.11º with a standard deviation of 1.51º. The sensors are more accurate over the areas where multiple sensors detect the electric field. When the electric field is in a direction where one sensor is close to the measurement noise floor the error increases. This can be seen in Figure 5-10 where the error increases at the extremes. If we limit

the detection band to $20^o < \theta < 70^o$ then the average error becomes 0.89^o for the xy measurement and 0.41^o for the xz measurement.

6 CONCLUSION

A directional SCOS sensor provides a compact method for determining the direction of an electric field. Three SCOS devices each detect a portion of the electric field which are used to determine the relative field direction. The design of the sensor allows it to be easy to interrogate and compact enough to fit into small areas such as on a circuit board. The sensor presented in this paper is able to detect the direction of an electric field with less than an average 1.26º.

6.1 Contributions

My main contributions presented in this work are in the area of multi-axial electric field sensing. These contributions are as follows:

- I fabricated and tested a three axis electric field sensor using three slab coupled optical sensors.
- I developed the use of Plexiglas in the use of packing SCOS.
- I developed a packaging technique that allows each sensor in a multi-axis SCOS sensor to be packaged separately making the overall sensor easier to align.
- I pioneered the use of x-cut KTP crystals in multi-axis sensors to decrease package size and increase usability.

- I contributed to the development of using electro-optic polymer as waveguides in SCOS devices.

6.1.1 Directional Electric Field Sensor

Contributions towards multi-axis SCOS sensing has been presented at in four technical conferences and has been published in one peer reviewed journal. Additionally two other papers have been submitted to peer reviewed journals for review. The contributions that are described in this work are as follows:

- I fabricated and tested a three axis electric field sensor using three slab coupled optical sensors.
  - Perry, D., Gibson, R., Schreeve, B., Schultz, S., Selfridge, D., "Multi-axial fiber-optic Electric field sensor," Proc. SPIE **7648**, 76480D, (2010).
  - Chadderdon, S., Perry, D., Van Wagoner, J., Selfridge, R., & Schultz, S. (2012). "Multi-axis, all-dielectric electric field sensors." *SPIE Conference Proceedings,* Baltimore*. , Vol. 8376 837608-837608-10.*
  - B. Shreeve, R. Gibson, D. Perry, R. Selfridge, S. Schultz, R. Forber, W. Wang, J. Luo, "Non-intrusive Field Characterization in Interior Cavities with Slab Coupled Optical Sensor (SCOS)," DEPS Conference, Albuquerque, NM, August 2010
  - Shreeve, B; Gibson, R.; Perry, D.; Selfridge, R.; Schultz, S.; Forber, R.; Wang, W.; Luo, J.; "Non-intrusive Field Characterization in Interior Cavities with Slab Coupled Optical Sensor (SCOS)," *Journal of Directed Energy* Vol. 4 No.2 2010.
  - Perry, D.; Chadderdon, S.; Forber, R.; Wang, W.; Selfridge, R.; Schultz, S. "*Multi-axis Electric Field Sensing using Slab Coupled Optical Sensors*" submitted to *Applied Optics*
  - Whitaker, B.; Noren, J.; Perry, D.; Schultz, S.; Selfridge, R.; Forber, R.; Wang, W.; Schleher, J. "The Application of SCOS for HPM Field Measurement" submitted to DEPS.

- I developed a packaging technique that allows each sensor in a multi-axis SCOS sensor to be packaged separately making the overall sensor easier to align.
    - Perry, D.; Chadderdon, S.; Forber, R.; Wang, W.; Selfridge, R.; Schultz, S. "*Multi-axis Electric Field Sensing using Slab Coupled Optical Sensors*" submitted to *Applied Optics*
- I pioneered the use of x-cut KTP crystals in multi-axis sensors to decrease package size and increase usability.
    - Perry, D.; Chadderdon, S.; Forber, R.; Wang, W.; Selfridge, R.; Schultz, S. "*Multi-axis Electric Field Sensing using Slab Coupled Optical Sensors*" submitted to *Applied Optics*
- I contributed to the development of using electro-optic polymer as waveguides in SCOS devices.
    - Perry, D.; Chadderdon, S.; Gibson, R.; Shreeve, B.; Selfridge, R.; Schultz, S.; Wang, W.; Forber, R.; Luo, J. (2011) "Electro-optic polymer electric field sensor," *SPIE Conference Proceedings,* San Diego, *Vol. 7982 79820Q-79820Q-8.*

6.1.2 Plexiglas Packaging

I developed the use of Plexiglas as packing for a SCOS. Using the laser cutter makes Plexiglas easy to fabricate and repeatable. Also there is less time commitment to make a Plexiglas trough because once the laser starts it can be left alone until the trough is finished. The Plexiglas packaging also is in a shape that allows for right angle mounting to other sensors which is valuable for making a multi-axis SCOS.

6.1.3 Individual Packaging for Directional Electric Field Sensors

Packaging each sensor individually makes the multi-axis SCOS sensor significantly easier to fabricate. Each sensor is made and packaged individually and then is glued to the others. Individual packaging allows broken SCOS to be replaced without damaging the other two allowing for less fabrication if a single SCOS breaks greatly increasing the reusability of the sensors. The use of individual packaging for each SCOS device is outlined in the SPIE conference proceeding *Multi-axial fiber-optic Electric Field Sensor* [26].

6.1.4 X-Cut KTP

Using an x-cut KTP crystal to detect electric fields in the z direction allows the packaging of the SCOS to be smaller. All three fibers can run parallel to each other significantly decreasing the overall size and ease of use of the sensor. Using x-cut KTP to reduce the size of the packaging is outlined in the paper submitted to *Applied Optics, Multi-axis Electric Field Sensing using Slab Coupled Optical Sensors*.

6.1.5 Polymer Waveguides

Using electro-optic polymer as the waveguide in SCOS devices creates a sensor that is more sensitive to electric fields than z-cut KTP but is also more difficult to fabricate. The theory behind why it is more sensitive and the process for fabrication is outlined in the SPIE conference publication *Electro-optic Polymer Electric Field sensor* [28].

6.2 Future Work

Directional electric field sensing using three SCOS sensors can still be improved on. The principles presented can each be improved upon to achieve better results. Smaller packaging would bring the sensing elements closer together increasing the special resolution of the sensor. Equipment cost can be reduced by making all three sensors at the same wavelength allowing them to be interrogated with a single tunable laser. Using only x-cut KTP for all three sensors could increase the sensitivity of the device due to boundary conditions changing the amount of electric field that drops over the slab waveguide.

6.2.1 Smaller Packaging for Increased Spatial Resolution

Using smaller packaging for the SCOS sensors would allow the three SCOS sensors to be closer together allowing for better special resolution. Currently the size of the packaging forces the slab waveguides to be about a 1.5 mm apart from each other setting the limit for the special resolution of the sensor. Smaller packaging reduces the spacing between the sensors increasing the special resolution.

6.2.2 Single Wavelength Sensor

The wavelength of the resonance dips for SCOS devices is dependent upon the thickness of the slab waveguide and refractive index of the slab waveguide. The effective refractive index of the waveguide can be changed in z-cut KTP by rotating the crystal on the D-fiber. This changes the location of the resonant dips.

Using this technique, three sensors can be fabricated to operate at the same wavelength allowing a single laser to be used in interrogation. The laser would be split into three parts and would then be used by each of the sensors as the light source.

6.2.3 All X-Cut Three-Axis SCOS

Due to boundary conditions, x-cut KTP is more sensitive to electric fields than z-cut KTP. Instead of using two z-cut crystals and an x-cut crystal, the three-axis SCOS can be fabricated with two lateral x-cut KTP SCOS and an x-cut SCOS with its optic axis parallel to the direction of the fiber. This would create a more sensitive multi-axis SCOS.

REFERENCES

1. A. E. Pevler, "Security implications of high-power microwave technology," in Proceedings of the 1997 International Symposium on Technology and Society, Piscataway, NJ, USA, 1997, pp. 107-111.

2. E. Van Keuren and J. Knighten, "Implications of the high-power microwave weapon threat in electronic system design," in *1991 IEEE International Symposium on Electromagnetic Compatibility*, Piscataway, NJ, USA, 1991, pp. 370-371.

3. C. R. Miller, "Electromagnetic Pulse Threats in 2010," United States, Report11 2005.

4. J. J. Foster, E. Gjelde, W. R. Graham, R. J. Hermann, and H. M. Kluepfel, "Report of the Commission to Assess the Threat to the United States from Electromagnetic Pulse (EMP) Attack. Volume 1: Executive Report," United States, Report 2004.

5. B. Yong-fang; L. Ying-hua; Z. Hong-xin; H. Chun-yuan; , "The analysis of shielding effectiveness of negative permittivity composite materials to different EMP," *Microwave, Antenna, Propagation and EMC Technologies for Wireless Communications, 2005. MAPE 2005. IEEE International Symposium on* , vol.1, no., pp.635-638 Vol. 1, 8-12 Aug. 2005 doi: 10.1109/MAPE.2005.1617991

6. C. E. Baum, E. L. Breen, J. C. Giles, J. O'Neill, and G. D. Sower, "Sensors for Electromagnetic Pulse Measurements Both Inside and Away from Nuclear Source Regions," *IEEE Transactions on Antennas and Propagation,* vol. 26, pp. 22-35, 1978.

7. *ACD D-DOT SENSOR (free field)*. Retrieved 9/25, 2012 from http://www2.urscorp.com/albuquerque/ACD-D-Dot(FreeField).htm

8. J. Ha, H. Jung. (2012). Integrated-optic electric field sensors utilizing ti:LiNbO3 mach-zehnder interferometric modulators. *Opto-Electronics and Communications Conference (OECC), 2012 17th,* 627-628.

9. S. Mathews, G. Farrell, Y. Semenova: All-fiber Polarimetric Electric Field Sensing Using Liquid Crystal Infiltrated Photonic Crystal Fiber. Sensors and Actuators A: Physical, Volume 167, Issue 1, Pages 54-59, 2011.

10. R. Gibson (2009). Slab coupled optical fiber sensors for electric field sensing applications. (Ph. D., Brigham Young University).

11. R. Forber, "Dielectric EM Field Probes for HPM Test & Evaluation," in *Annual ITEA Technology Review*, Cambridge, MA, 2006.

12. S. Haishan, P. Anna, L. Jingdong, S. Zhengwei, H. Steven, K. Y. J. Alex, R. D. Larry, and C. Antao, "All-Dielectric Electrooptic Sensor Based on a Polymer Microresonator Coupled Side-Polished Optical Fiber," *IEEE Sensors Journal,* vol. 7, pp. 515-524, 2007.

13. W. C. Wang, W. Lin, H. Marshall, R. Skolnick, and D. Schaafsma, "All-dielectric miniature wideband rf receive antenna," *Optical Engineering,* vol. 43, pp. 673-677, 2004.

14. H. Sun, A. Pyajt, J. Luo, Z. Shi, S. Hau, A. Jen, L. Dalton, and A. Chen, "Broadband electric field sensor with electro-optic polymer micro-ring resonator on side-polished optical fiber," San Jose, CA, United states, 2006, p. SPIE.

15. S. A. Hamilton, D. R. Yankelevich, A. Knoesen, R. T. Weverka, R. A. Hill, and G. C. Bjorklund, "Polymer in-line fiber modulators for broadband radio-frequency optical links," *Journal of the Optical Society of America B: Optical Physics,* vol. 15, pp. 740-750, 1998.

16. *Operation guide for different free-field D-dot sensors.* (2009). Retrieved 5/21, 2012, from http://prodyntech.com/home/page/operation_guide_for_different_free_field_d_dot_sensors

17. M. A. Jensen and R. H. Selfridge, "Analysis of etching-induced birefringence changes in elliptic core fibers," Appl. Opt. 31, 2011-2016 (1992).

18. C. A. Millar, M.C. Brierley and S.R. Mallinson, "Exposed-core single-mode-fiber channel-dropping filter using a high index overlay waveguide," OPT. Lett. 12, 284-286 (1987).

19. W. B. Jones (1988). *Introduction to optical fiber communication systems*. New York: Holt, Rinehart and Winston, Inc.

20. S. Chadderdon, R. Gibson, R. H. Selfridge, S. M. Schultz, W. C. Wang, R. Forber, J. Lou, and A.K.Y. Jen, "Optimal crystal geometry and orientation in electric field sensing using electro-optic sensors" Appl. Opt. **50**, 3505 (2011).

21. V. Ramaswamy, "Propagation in asymmetrical anisotropic film waveguides," Appl. Opt. 13, 1363–1371 (1974).

22. D. L. Lee, "Electromagnetic principles of integrated optics," New York: Wiley, 1986, p. 227.

23. B. Shreeve (2011). Magnetic field sensing with slab coupled optical fiber sensors. (Master's, Brigham Young University).

24. S. Chadderdon, R. Gibson, R. Selfridge, S. Schultz, W. Wang, R. Forber, J. Lou, A. Jen (2011). Electric-field sensors utilizing coupling between a D-fiber and an electro-optic polymer slab. *Applied Optics, 50* (20), 3505-3506-3512.

25. E. Van Tomme, P. Van Daele, P. Baets, P. Lagasse. (1991). Integrated optic devices based on nonlinear optical polymers. *IEEE Journal of Quantum Electronics, 27*(3), 778-779-787.

26. D. Perry, R. Gibson, B. Schreeve, S. Schultz, D. Selfridge, "Multi-axial fiber-optic Electric field sensor," Proc. SPIE **7648**, 76480D, (2010).

27. ***Telecommunications: Glossary of telecommunication terms*** (1991). General Services Administration Information Technology Service.

28. D. Perry, S. Chadderdon, R. Gibson, B. Shreeve, R. Selfridge, S. Schultz, W. Wang, R. Forber, J. Luo (2011) "Electro-optic polymer electric field sensor," *SPIE Conference Proceedings,* San Diego, *Vol. 7982 79820Q-79820Q-8.*

APPENDIX A. LASER CUTTER SETTINGS

To program the laser cutter a stencil is used. Each color in the stencil can be programmed to a different laser speed and intensity. Figure A-1 shows the stencil used to cut out the trough.

Figure A-1: Stencil for the laser cutter at the BYU Electrical Engineering shop. The width is 5 cm and the height is 0.4 cm.

The settings for each color are:

Black: Air assist on, Engrave, Power 100%, Speed 6%

Red: Air assist on, Engrave, Power 100%, Speed 10%

Green: Air assist on, Engrave, Power 20%, Speed 1%

Blue: Air assist on, Engrave, power 20%, Speed 1%

These settings will cut out a trough from a solid piece of Plexiglas.

APPENDIX B. X-CUT SCOS FABRICATION

Fabricating an x-cut KTP SCOS is similar to z-cut but the crystal orientation needs to be accounted for. As seen in Figure B-1a the crystal should be orientated by with the optic axis parallel to the optical fiber. This requires special attention when fabricating the SCOS so that the crystal does not rotate or get flipped during fabrication.

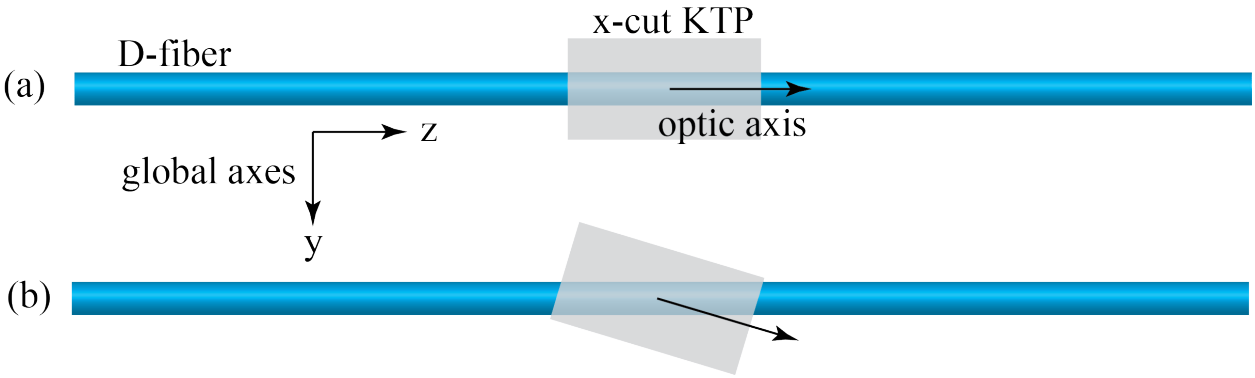

Figure B-1: (a) Correct alignment for an x-cut KTP crystal with the optic axis parallel to the fiber direction (b) Incorrect alignment for an x-cut KTP crystal

Figure B-1b shows a common error when fabricating an x-cut SCOS. The crystal is rotated causing the optic axis to offset from the fiber resulting in a SCOS that is sensitive to electric fields that are not parallel to the fiber. This makes it more difficult to correctly align the three axis sensor.